The Astrophysical Journal, 1012:154 (23pp), 2026 November 20 https://doi.org/10.3847/1538-4357/aeb265
© 2026. The Author(s). Published by the American Astronomical Society.
OPEN ACCESS

Deciphering the Physical Origin of GRB 240825A: A Long Gamma-Ray Burst Lacking a Bright Supernova

Rahul Gupta[1,46], Judith Racusin[1], R. Sánchez-Ramírez[2], Y.-D. Hu[3,4], A. Rossi[5], M. D. Caballero-García[2], Pi Nuessle[1,6], A. J. Castro-Tirado[2,7], S. R. Oates[8], P. P. Bordoloi[9], A. Aryan[10], S. Dichiara[11], P. Veres[12,13], N. Klingler[1], N. Omodei[14], E. Maiorano[5], D. Tak[15], S. Shilling[8], J. E. Adsuara[16], P. H. Connell[16], E. Fernández-García[2], G. García-Segura[2,17], A. Ghosh[18], E. Göğüş[19], F. J. Gordillo-Vázquez[2], M. Gritsevich[20,21,22], A. Nicuesa Guelbenzu[23], S. Guziy[2,24,25], L. Hanlon[26], H. J. van Heerden[27], S. Iyyani[9,28], A. Martin-Carrillo[26], P. J. Meintjes[27], J. Navarro-González[16], T. Neubert[29], N. Østgaard[30], S. B. Pandey[31], I. Pérez-García[2], S. Razzaque[6,18,32], E. Sonbas[6], Si-Yu Wu[2], A. Pozanenko[33], A. Volnova[34], A. Moskvitin[35], S. Belkin[36], O. Spiridonova[35], O. Burkhonov[37], Sh. Egamberdiyev[37,38], E. Klunko[39], V. Rumyantsev[40], I. Sokolov[41], A. Novichonok[42], I. Reva[43], A. Volvach[40], L. Volvach[40], Jan Snigula[44], and Chiara Ventura[45]

[1] Astrophysics Science Division, NASA Goddard Space Flight Center, Mail Code 661, Greenbelt, MD 20771, USA; rahul.gupta@nasa.gov, rahulbhu.c157@gmail.com
[2] Instituto de Astrofísica de Andalucía (IAA-CSIC), Glorieta de la Astronomía s/n, E-18008, Granada, Spain
[3] Guangxi Key Laboratory for Relativistic Astrophysics, School of Physical Science and Technology, Guangxi University, Nanning 530004, People's Republic of China
[4] INAF—Osservatorio Astronomico di Brera, Via E. Bianchi 46, 23807, Merate, LC, Italy
[5] INAF—Osservatorio di Astrofisica e Scienza dello Spazio, Via Piero Gobetti 93/3, 40129 Bologna, Italy
[6] Department of Physics, The George Washington University, 725 21st Street NW, Washington, DC 20052, USA
[7] Ingeniería de Sistemas y Automática, Universidad de Málaga, Unidad Asociada al CSIC porel IAA, Escuela de Ingenierías Industriales, Arquitecto Francisco Peñalosa, 6, Campanillas, 29071, Málaga, Spain
[8] Department of Physics, Lancaster University, Lancaster, LA1 4YB, UK
[9] Indian Institute of Science Education and Research, Thiruvananthapuram, Kerala 695551, India
[10] Graduate Institute of Astronomy, National Central University, 300 Jhongda Road, 32001, Jhongli, Taiwan
[11] Department of Astronomy and Astrophysics, Pennsylvania State University, 525 Davey Lab, University Park, PA 16802, USA
[12] Department of Space Science, University of Alabama in Huntsville, Huntsville, AL 35899, USA
[13] Center for Space Plasma and Aeronomic Research, University of Alabama in Huntsville, Huntsville, AL 35805, USA
[14] SLAC National Accelerator Laboratory, Stanford University, Stanford, CA 94305, USA
[15] Department of Physics, Kyung Hee University, Seoul 02447, Republic of Korea
[16] Image Processing Laboratory, University of Valencia, Paterna, Valencia, Spain
[17] Instituto de Astronomía, Universidad Nacional Autónoma de México, Carr. Tijuana-Ensenada km.107, 22860, Ensenada, B.C., Mexico
[18] Centre for Astro-Particle Physics (CAPP) and Department of Physics, University of Johannesburg, PO Box 524, Auckland Park 2006, South Africa
[19] Faculty of Engineering and Natural Sciences, Sabancı University, Istanbul 34956, Türkiye
[20] Swedish Institute of Space Physics (IRF), Bengt Hultqvists väg 1, 981 92 Kiruna, Sweden
[21] University of Helsinki, Faculty of Science, Gustav Hällströmin katu 2, FI-00014, Finland
[22] Institute of Physics and Technology, Ural Federal University, Mira str. 19, 620002, Ekaterinburg
[23] Thüringer Landessternwarte Tautenburg, Sternwarte 5, 07778 Tautenburg, Germany
[24] Petro Mohyla Black Sea National University, Mykolaiv 54000, Ukraine
[25] Mykolaiv Astronomical Observatory, Mykolaiv 54030, Ukraine
[26] School of Physics and Centre for Space Research, University College Dublin, Belfield, Dublin 4, Ireland
[27] Department of Physics, University of the Free State, 205 Nelson Mandela Drive, Bloemfontein, 9300, South Africa
[28] High Performance Computing Centre, IISER Thiruvananthapuram, Kerala, 695551, India
[29] National Space Institute, Technical University of Denmark, Kgs. Lyngby, Denmark
[30] Birkeland Centre for Space Science, Department of Physics and Technology, University of Bergen, Bergen, Norway
[31] Aryabhatta Research Institute of Observational Sciences (ARIES), Manora Peak, Nainital 263002, India
[32] National Institute for Theoretical and Computational Sciences (NITheCS), Private Bag X1, Matieland, South Africa
[33] Faculty of Physics, Higher School of Economics, Moscow 101000, Russia
[34] Sternberg Astronomical Institute, Moscow State University, Moscow Russia
[35] Special Astrophysical Observatory, Russian Academy of Sciences, Nizhny Arkhyz 369167, Russia
[36] School of Physics & Astronomy, Monash University, Clayton VIC 3800, Australia
[37] Ulugh Beg Astronomical Institute, Uzbek Academy of Sciences, Tashkent 100052, Uzbekistan
[38] National University of Uzbekistan, Tashkent, Uzbekistan
[39] Institute of Solar-Terrestrial Physics, Russian Academy of Sciences (Siberian Branch), Irkutsk 664033, Russia
[40] Crimean Astrophysical Observatory, Russian Academy of Sciences, Nauchny 298409, Crimea[†]
[41] Institute of Astronomy of the Russian Academy of Sciences, Moscow, Russia
[42] Petrozavodsk State University, 185910, Petrozavodsk, Karelia, Russia
[43] Fesenkov Astrophysical Institute, Observatory Street 23, Almaty 050020, Kazakhstan
[44] Max-Planck-Institut für Extraterrestrische Physik, Giessenbachstraße 1, 85748 Garching, Germany

[45] INAF–Osservatorio Astronomico di Roma, via Frascati 33, I-00040 Monte Porzio Catone, Italy
Received 2025 July 31; revised 2026 August 20; accepted 2026 September 22; published 2026 November 18

Abstract

We present a comprehensive multiwavelength analysis of GRB 240825A, a bright gamma-ray burst (GRB) detected by Fermi and Swift, with a prompt duration ($T_{90} \sim 4$ s in the 50–300 keV band measured by the Gamma-ray Burst Monitor) near the boundary separating short and long GRBs, prompting a detailed investigation into its classification and progenitor. We use classical prompt metrics (duration, minimum variability timescale, lag, and spectral hardness) and modern classification techniques (machine learning–based t-SNE, support vector machine, energy- hardness duration, and $\varepsilon \equiv E_{\gamma,\mathrm{iso},52}/E^{5/3}_{p,z,2}$) and find most properties (prompt energetics, placement on the Amati relation, and spectral lag) of GRB 240825A consistent with a collapsar origin. However, extensive late-time optical and near-infrared follow-up with the 10.4 m Gran Telescopio Canarias (GTC) telescope and the 8.4 m Large Binocular Telescope reveals no bright supernova (SN; like SN 1998bw) is detected down to stringent limits (e.g., $m_r > 25.0$ mag at 17.59 days), despite a redshift of $z = 0.659$ measured from GTC spectroscopy. Host-galaxy spectral energy distribution modeling with `Prospector` indicates a massive, star-forming galaxy typical of collapsar GRB hosts, though with a large offset. We compare these findings with hybrid events like GRB 211211A, GRB 230307A, GRB 200826A, including supernovae-GRBs, and conclude that GRB 240825A most likely originated from a massive star collapse, possibly with the associated AN heavily obscured or intrinsically faint. This study emphasizes the need for multiwavelength follow-up and a multilayered classification to determine GRB progenitors.

Unified Astronomy Thesaurus concepts: Gamma-ray bursts (629); High energy astrophysics (739)

1. Introduction

Gamma-ray bursts (GRBs) are broadly divided into two main classes—short and long—based on their observed durations (T_{90}, the time interval containing 90% of the burst's fluence, C. Kouveliotou et al. 1993) and spectral hardness (A. Lien et al. 2016). This dichotomy, first revealed by the Burst and Transient Source Experiment (BATSE) on board the Compton Gamma Ray Observatory, has served as a foundation for understanding GRB progenitors. Long-duration GRBs ($T_{90} > 2$ s) typically have softer photon spectra than short-duration GRBs ($T_{90} \leqslant 2$ s).

The physical association of long-duration GRBs with the core collapse of massive, rapidly rotating stars (S. E. Woosley 1993; A. I. MacFadyen & S. E. Woosley 1999), sometimes accompanied by broad-lined Type Ibc supernovae (SNe; J. Hjorth et al. 2003; S. E. Woosley & J. S. Bloom 2006), and short-duration GRBs with compact binary mergers such as binary neutron star or neutron star-black hole systems (E. Nakar 2007; E. Berger 2014), provided an initial physical basis for the T_{90}-based dichotomy. However, the T_{90}-based classification scheme has significant limitations. The duration of a GRB is not a purely intrinsic property but is instead dependent on the energy band of the detector, the sensitivity threshold, the signal-to-noise ratio (S/N) of the event, and the redshift of the source (O. Bromberg et al. 2013; Y. Qin et al. 2013; M. Moss et al. 2022). For instance, T_{90} tends to be longer at lower energies, and bursts with extended soft tails may be misclassified as long GRBs when observed with sensitive instruments like the Swift Burst Alert Telescope (BAT). Such instrumental dependencies introduce ambiguities, particularly for GRBs near the empirical boundary of $T_{90} \sim 2$ s. Moreover, the observed duration distributions of short and long GRBs significantly overlap, further complicating the classification of events near this boundary.

The complexity has only increased with the discovery of more such ambiguous or "hybrid" events. For example, GRB 060614, a long-duration GRB ($T_{90} \sim 100$ s), showed no accompanying supernova (SN) emission down to deep optical limits (M. Della Valle et al. 2006; N. Gehrels et al. 2006), challenging the long-duration GRB/SN association. J. P. U. Fynbo et al. (2006) reported another nearby long-duration GRB, GRB 060505, with T_{90} values of 4 s, that exhibited no SN emission down to limits hundreds of times fainter than SN 1998bw (a prototypical GRB-SN). These nearby "SN-less" GRBs, located in star-forming regions, suggest that not all long GRBs conform to the collapsar model. More recently, long-duration GRBs like GRB 191019A, GRB 211211A, GRB 211227A, and GRB 230307A exhibit signatures (e.g., kilonova (KN)-like emission) consistent with compact binary mergers (H.-J. Lü et al. 2022; J. C. Rastinejad et al. 2022; E. Troja et al. 2022; J. Yang et al. 2022; A. J. Levan et al. 2024; Y.-H. Yang et al. 2024; G. Stratta et al. 2025). Conversely, a short-duration burst GRB 200826A, despite $T_{90} \lesssim 2$ s, is associated with young, star-forming environments and an SN component, suggesting a collapsar origin (T. Ahumada et al. 2021; A. Rossi et al. 2022). These events highlight that duration alone is not a reliable proxy for progenitor type (O. Bromberg et al. 2013; B. Zhang 2025).

Such hybrid events inspired the development of physically motivated classification systems such as the "Type I (associated with the mergers of compact objects)/Type II (associated with the collapsars)" scheme (B. Zhang et al. 2009), which incorporates prompt emission, afterglow, host galaxy properties, local environments, and the presence (or absence) of SNe. To overcome the limitations of duration-based classification, the community increasingly employs multiwavelength and multi-dimensional analyses. Key discriminants include prompt emission properties such as spectral lag (J. P. Norris et al. 2000), and

[46] NASA Postdoctoral Program Fellow.

[†] While the AAS journals adhere to and respect UN resolutions regarding the designations of territories (available at http://www.un.org/press/en), it is our policy to use the affiliations provided by our authors on published articles.

Original content from this work may be used under the terms of the Creative Commons Attribution 4.0 licence. Any further distribution of this work must maintain attribution to the author(s) and the title of the work, journal citation and DOI.

minimum variability timescale (MVT; G. A. MacLachlan et al. 2013; A. E. Camisasca et al. 2023), afterglow properties (M. G. Dainotti et al. 2020; A. Lenart et al. 2025), as well as host galaxy properties such as morphology, star formation rate (SFR), and metallicity (A. S. Fruchter et al. 2006; W.-f. Fong et al. 2022; R. Gupta et al. 2022b). Furthermore, machine learning (ML) techniques have been leveraged to integrate these diverse observational parameters into more robust, probabilistic classification frameworks (C. K. Jespersen et al. 2020; J.-W. Luo et al. 2023; P. Nuessle et al. 2024; S.-Y. Zhu et al. 2024; M. Negro et al. 2025).

In this study, we present a comprehensive multiwavelength investigation (classical and ML-based) of GRB 240825A, a long-duration event ($T_{90} \sim 4$ s) detected by Fermi. We examine the prompt emission characteristics (including ML-based classification), afterglow temporal and spectral evolution, and host galaxy properties to establish its classification and physical origin. We used the 10.4 m Gran Telescopio Canarias (GTC) telescope and the Large Binocular Telescope (LBT) to search for an associated SN and decipher the physical origin of GRB 240825A. Despite extensive monitoring, no SN emission is detected, reminiscent of GRBs 060505, 060614, and GRB 111005A (M. J. MichałowskI et al. 2018; M. Tanga et al. 2018). The available limits provide only mild constraints. They mainly disfavor a luminous SN 1998bw-like component at the epochs covered, while fainter or more dust-obscured GRB-SNe remain possible. Section 2.1 presents the observations and data analysis, Section 3 details the results, and Section 4 discusses the physical interpretation of the results. Conclusions are drawn in Section 5.

2. Observations and Data Analysis

2.1. Prompt Emission Detection

GRB 240825A was detected by the Fermi Gamma-ray Burst Monitor (GBM) at 15:53:00 UTC on 2024 August 25 (Fermi GBM Team 2024). The burst was also detected by the Fermi Large Area Telescope, which detected significant high-energy emission above 100 MeV (N. Di Lalla et al. 2024). The Swift BAT independently triggered on GRB 240825A at 15:52:59 UTC, localizing the burst to coordinates R.A. (J2000) = $22^h58^m12.^s$, decl. (J2000) = +01d 02′ 10″ with an uncertainty of 3′ (R. Gupta et al. 2024a). We carried out the temporal analysis of the Swift-BAT data of GRB 240825A (see method in R. Gupta et al. 2025). The mask-weighted light curve (binned at 128 ms in the 15–350 keV band), displayed in Figure 1, shows a bright, fast-rising, exponential decay–like main prompt emission pulse, starting at T_0 s (Swift BAT trigger time), peaking at T_0 +1.8 s, and ending at T_0 +10 s. To further probe for any extended emission (EE), we constructed a light curve with S/N criteria with 5 or 10 s binning, which uncovers faint emission persisting beyond the main-emission phase. This softer and longer tail emission extends up to $\sim T_0 + 300$ s with a T_{90} duration of 57.20 ± 8.57 s (M. J. Moss et al. 2024). We further compared GRB 240825A's 25–50 keV and 50–100 keV fluence to a sample of Swift-BAT and BATSE GRBs, finding its fluence ($\sim 10^{-5}$ erg cm^{-2}) to be high (see Figure 1).

2.2. X-Ray Afterglow

The Swift X-Ray Telescope (XRT; D. N. Burrows et al. 2005) initiated observations of the GRB 240825A field at 15:54:22.9 UT, approximately 83.1 s after the Swift-BAT trigger. The XRT identified a bright, uncatalogued, and fading X-ray source at R. A. = 22h 58 m 16.58 s, decl. = +01d 01′ 31.″1 (J2000), with a

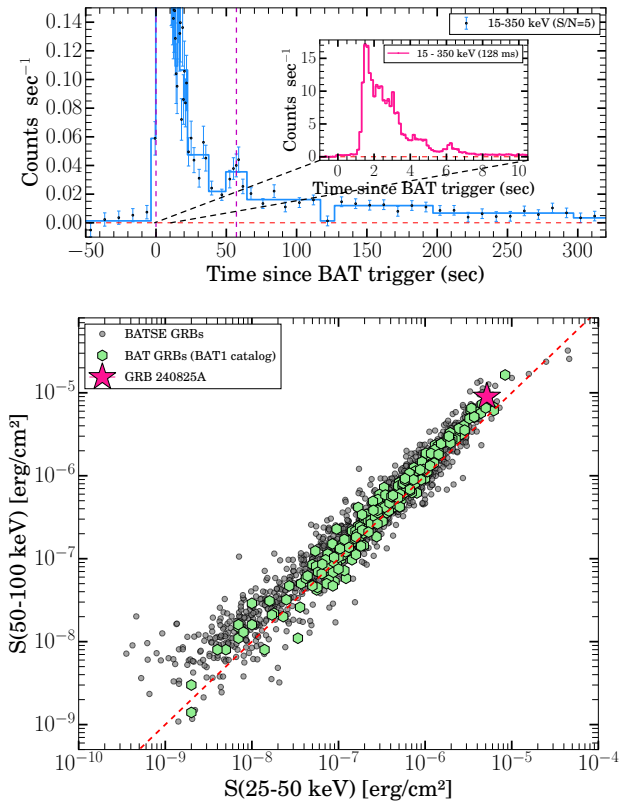


Figure 1. Top: BAT light curve in the 15–350 keV energy range reveals the presence of a faint EE post the main burst, observed after employing S/N criteria with 5 or 10 s binning. The vertical dashed lines represent a BAT T_{90} duration of 57.20 s. The inset shows the prompt zoomed light curve of GRB 240825A in the 15–350 keV energy range, observed using the Swift-BAT and presented in 128 ms time bins, which highlights the burst's immediate temporal behavior. Bottom: the comparative analysis of GRB 240825A's fluence (pink star) with other GRBs detected by the BAT and BATSE instruments, https://swift.gsfc.nasa.gov/results/batgrbcat/, showing its high fluence ($\sim 10^{-5}$ erg cm^{-2}), typically consistent with collapsar GRBs. The red dashed line marks that the fluence in the S (50–100 keV) band is equal to the fluence in the S (25–50 keV) band.

positional uncertainty of 12.″3 (90% containment), and further, an astrometrically corrected position was determined at R.A. = 22^h 58^m $17.28.^s$, decl. = +01d 01′ 36.″3 (J2000), with a refined uncertainty of 2.″7 (90% confidence). This position lies 75″ from the BAT onboard location (P. A. Evans et al. 2024). Temporal and spectral data for the X-ray afterglow were retrieved from the Swift-XRT GRB light curve and spectrum repositories (P. A. Evans et al. 2007; P. A. Evans et al. 2009), provided by the UK Swift Science Data Centre.[47] The XRT spectrum in the 0.3–10 keV energy range was fitted with an absorbed power-law model, using both a fixed Galactic absorption model (`phabs`) and a free absorption model (`zphabs`) to constrain contributions from the host galaxy (see R. Gupta 2023; A. J. Castro-Tirado et al. 2024 for detailed methodology).

2.3. Ultraviolet and Optical Observations

2.3.1. Swift-UVOT

The Swift-UVOT (P. W. A. Roming et al. 2005) began observations of the field of GRB 240825A (N. P. M. Kuin et al. 2024) 77 s after the Swift-BAT trigger. The source counts

[47] https://www.swift.ac.uk/

were extracted using a source region of 5″ radius. Background counts were extracted using a 20″ circular region located in a source-free region. The afterglow count rates were converted to magnitudes using the UVOT photometric zero-points (T. S. Poole et al. 2008; A. A. Breeveld et al. 2011). To improve the S/N ratio, the count rates in each filter were binned using $\Delta t/t = 0.2$. The UVOT detector is less sensitive in a few small patches[48] for which a correction has not yet been determined. Therefore, we determine if the afterglow falls on any of these patches. We find that during the *white*, *u*, and UV filters during the first 1300 s, the afterglow does fall on one of these patches. We have therefore excluded the UV data affected by this, but we include *white* and *u*-band data since it provides information on the early time behavior of the afterglow; as such, caution should be used when interpreting the early *white* and *u*-band data. The Swift-UVOT observations of GRB 240825A are detailed in Table A1 of the Appendix.

2.3.2. Observatorio de Sierra Nevada and BOOTES

We conducted optical afterglow observations of GRB 240825A using the 1.5 m telescope at the Observatorio de Sierra Nevada (OSN) in Spain and the 0.6 m Dolores Pérez-Ramírez robotic telescope (DPRT) at the BOOTES-6 station in South Africa (as part of the BOOTES Global Network, A. J. Castro-Tirado 2023; Y. D. Hu et al. 2023). OSN observations began approximately 8.4 hr ($T - T_0 = 30{,}176$ s) post-trigger, covering the *B*, *V*, *I*, and *R* bands. The OSN data were reduced with a custom pipeline that included bias subtraction, flat-field correction using flat frames, and background subtraction to account for varying sky conditions. Aperture photometry, optimized for the afterglow's point-spread function, was calibrated against nearby Pan-STARRS1 stars to derive AB magnitudes, reported without corrections for Galactic or host extinction (see Table A1 of the Appendix). Complementary *R*-band observations were obtained with the 0.6 m BOOTES-6/DPRT starting approximately 2.5 hr ($T - T_0 =$ 9063 s) post-trigger. BOOTES-6 data were reduced with bias and flat-field corrections and initially calibrated to the Vega magnitude system. These magnitudes were converted to the AB system using a zero-point offset of 0.21 mag.

2.3.3. GRB IKI-FuN Observations

We continued monitoring the afterglow using a range of telescopes from the IKI Gamma-Ray Burst Follow-up Network (IKI GRB-FuN network; A. Volnova et al. 2021) and additional facilities. Optical observations were conducted with the 1.5 m AZT-22 telescope at the Maidanak Astronomical Observatory, operated by the Ulugh Beg Astronomical Institute in Uzbekistan. Further *R*-band imaging was obtained with the Zeiss-1000 telescope, located at the Special Astrophysical Observatory (SAO) in Russia. Additional observations were carried out using the RC-35 (Kitab) and the Zeiss-1000 telescopes. All our optical data obtained from the IKI GRB-FuN network were processed using NOAO's IRAF software package.[49] Results of the observations are presented in Table A1 of the Appendix.

[48] https://heasarc.gsfc.nasa.gov/docs/heasarc/caldb/swift/docs/uvot/uvotcaldb_sss_02b.pdf

[49] https://iraf-community.github.io/

2.4. Late-time Imaging and Spectroscopy: Search for SN and Host Galaxy

2.4.1. 10.4 m GTC Spectroscopy Observations and Redshift Determination

We performed spectroscopic observations of the field of GRB 240825A using the Optical System for Imaging and low-Intermediate-Resolution Integrated Spectroscopy (OSIRIS) mounted on the 10.4 m GTC, located at the Roque de los Muchachos Observatory, La Palma, Canary Islands. Observations were conducted on 2024 October 9 and 10 under good atmospheric conditions, with airmass ranging from 1.13 to 1.25. We used the R1000B grism, which covers the wavelength range of 3630–7500 Å with a spectral resolving power of $R \sim 1000$.

Data reduction was performed using standard IRAF routines and complementary Python-based tools. The two-dimensional spectroscopic frames were bias-subtracted, flat-field corrected, and cleaned of cosmic rays using the `L.A. Cosmic` algorithm (P. G. van Dokkum 2001). One-dimensional spectra were extracted using an optimal aperture centered on the galaxy trace after subtracting the background via a low-order polynomial fit to spatial regions adjacent to the target. Wavelength calibration was achieved using comparison arc lamps (Ne, Ar, and Hg), and flux calibration was performed using a spectrophotometric standard star (Feige110) observed on the same nights. Finally, we accounted for slit losses (∼29%) by scaling the spectrum to the photometric magnitude measured in the *r*′ band (see detailed methodology in Y. D. Hu et al. 2021; R. Gupta et al. 2022a; R. Sánchez-Ramírez et al. 2024).

The reduced and calibrated spectrum (Figure 2) exhibits prominent [O II] λλ3727, 3729 emission lines associated with the host galaxy, as well as several absorption features including Ca II H, Ca II K, the *G* band, Ca I λ4227, Sr II λ4077, CN λ3883, and multiple Fe II, Fe I and Mg II lines. These lines were consistently identified across both nights, yielding a redshift measurement of $z = 0.659$ for the host galaxy of GRB 240825A. Our redshift measurement is consistent with the value measured by the VLT equipped with the X-shooter spectrograph (A. Martin-Carrillo et al. 2024). We also noted several foreground (Milky Way) features (see Figure 2) in our spectrum.

2.4.2. 10.4 m GTC Near-infrared and Optical Panchromatic Observations

We performed near-infrared (NIR) and optical imaging observations of the host galaxy of GRB 240825A using the 10.4 m GTC, equipped with the OSIRIS instrument for optical bands and the Espectrógrafo Multiobjeto Infra-Rojo (EMIR) instrument for NIR bands. Optical imaging was conducted in the *g*, *r*, *i*, and *z* filters, starting approximately 104 days after the GRB trigger. NIR observations in the *J*, *H*, and *K* bands were obtained spanning a temporal range of ∼19.31–27.41 days post-trigger. The raw data were processed using the standard pipeline, which included bias subtraction, flat-fielding, and sky subtraction tailored to the varying background levels in each band. Photometry was performed using aperture photometry with a radius optimized for the host's point-spread function (see R. Gupta et al. 2021 for detailed methodology). Optical AB magnitudes were calibrated against Pan-STARRS standard stars, while NIR magnitudes were

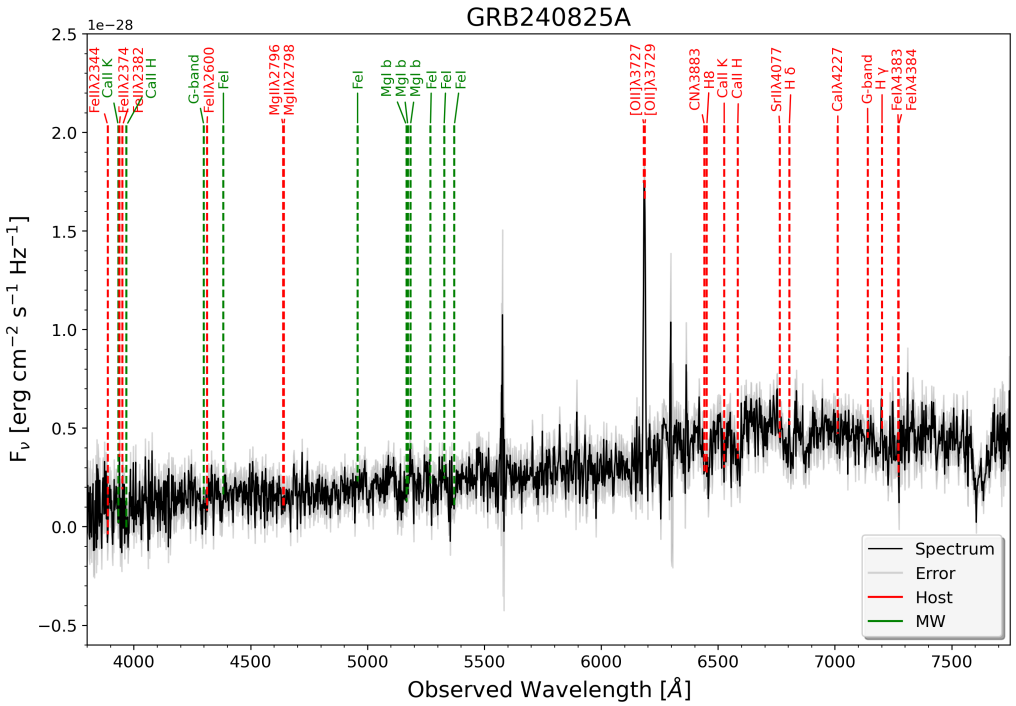


Figure 2. Optical spectrum of the host galaxy of GRB 240825A obtained with the 10.4 m GTC. The spectrum (black) is overlaid with the corresponding error spectrum (gray). Features associated with the host galaxy are marked in red, while foreground (Milky Way) features are shown in green. Detected lines include [O II] $\lambda\lambda$3727, 3729, Ca II H, Ca II K, and several Fe II, Mg II, and Balmer lines, which were used to determine a redshift of $z = 0.659$ for the host galaxy.

calibrated using Two Micron All Sky Survey standards. These magnitudes are reported without corrections for Galactic or host extinction (see Table 1).

2.4.3. Dark Energy Spectroscopic Instrument Optical Infrared Observations

Complementing GTC host observations, we extracted multiband photometry from the Dark Energy Spectroscopic Instrument (DESI) Legacy Surveys Data Release 10 (DR10), covering the g, r, i, z, W1, W2, and W3 bands, using the survey's public catalog. For the data analysis of DESI data, we performed aperture photometry with a radius optimized to the host's point-spread function, calibrated against Pan-STARRS standard stars for optical bands (g, r, i, z) and WISE standards for infrared bands (W1, W2, W3). The resulting magnitudes were derived without applying reddening corrections and are summarized in Table 1. We noted that GTC optical measurements remain consistent with DESI values.

2.4.4. 2.2 m CAHA Optical Observations

We also obtained observations with the 2.2 m telescope at the Calar Alto Observatory in Almería, Spain, using the Calar Alto Faint Object Spectrograph. Imaging was performed in the Sloan g', r', i', and z' filters on two epochs: 2024 September 28 and 2024 November 24. However, only the data from the first night were usable due to poor weather conditions during the second epoch. The first observation began at 21:31 UT, corresponding to approximately 34 days postburst. A faint detection of the GRB host galaxy was noted in the stacked images (see Table 1). The raw data were reduced using standard procedures. Absolute photometric calibration was performed using nearby field stars from the Pan-STARRS1 catalog.

Table 1
Host Galaxy Photometric Observations of GRB 240825A

Instrument/Survey	Filter/Band	$T - T_0$ (s)	Exp. (s)	AB Mag ± error
GTC Optical Imaging				
GTC	r	9,004,750	540	22.45 ± 0.07
GTC	g	9,005,075	960	23.76 ± 0.11
GTC	i	9,005,502	540	22.03 ± 0.05
GTC	z	9,006,216	400	21.63 ± 0.12
GTC NIR Imaging				
GTC	K	1,668,561	1260	21.10 ± 0.06
GTC	J	1,671,315	910	21.77 ± 0.10
GTC	H	1,673,259	1134	21.50 ± 0.09
GTC	K	2,365,811	1260	21.14 ± 0.06
GTC	J	2,368,461	910	21.81 ± 0.14
DESI Legacy Surveys (DR10)				
DESI	g	⋯	⋯	23.607 ± 0.063
DESI	r	⋯	⋯	22.463 ± 0.027
DESI	i	⋯	⋯	21.875 ± 0.051
DESI	z	⋯	⋯	21.627 ± 0.032
DESI	W1	⋯	⋯	20.577 ± 0.102
DESI	W2	⋯	⋯	21.692 ± 0.965
DESI	W3	⋯	⋯	18.141 ± 1.322
CAHA Optical Imaging				
CAHA	g	2,961,761	750	23.53 ± 0.20
CAHA	r	2,960,729	720	22.71 ± 0.14
CAHA	i	2,959,660	720	21.78 ± 0.15
CAHA	z	2,958,492	700	21.87 ± 0.29

Note. AB magnitudes are reported without corrections for Galactic or host extinction. For GTC observations, $T - T_0$ represents the time since the GRB trigger, and Exp. is the exposure time. DESI Legacy Surveys data are from DR10, with no reddening correction applied.

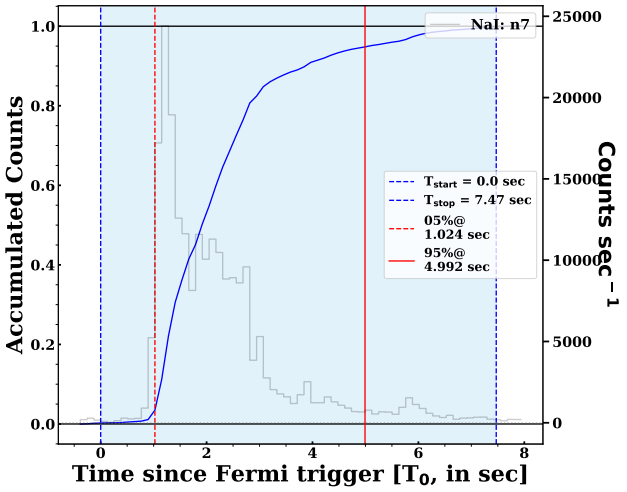


Figure 3. Cumulative count rate and T_{90} calculation for GRB 240825A in Fermi-GBM 50–300 keV depicting the cumulative count rate of GRB 240825A as observed by the Fermi-GBM in the 50–300 keV energy band, with time measured relative to the GBM trigger. The T_{90} duration, representing the interval containing 90% of the burst's fluence, is calculated as 3.968 s, defined by the 5% accumulation level at 1.024 s (red dashed line) and the 95% level at 4.992 s (red solid line), with a start time of 0.0 s and stop time of 7.47 s (blue dashed lines). The background-subtracted cumulative profile, shown in blue, illustrates the burst's temporal evolution, with the T_{90} value of $\sim$ 2 s suggesting an ambiguous classification. The background-subtracted GBM light curve is shown in gray.

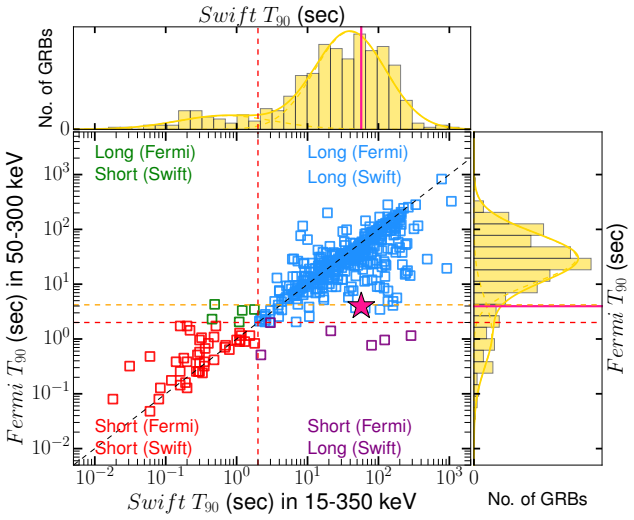


Figure 4. Scatter plot of Swift T_{90} vs. Fermi T_{90} durations for GRBs detected by both instruments. GRBs are classified into four categories: pure long (both $T_{90} > 2$ s, blue squares), pure short (both $T_{90} \leqslant 2$ s, red squares), Fermi long–Swift short (Fermi $T_{90} > 2$ s, Swift $T_{90} < 2$ s, green squares), and Swift long–Fermi short (Swift $T_{90} > 2$ s, Fermi $T_{90} < 2$ s, purple squares). GRB 240825A is highlighted as a pink star with error bars (Swift $T_{90} = 57.20 \pm 8.57$ s, Fermi $T_{90} = 3.968 \pm 0.091$ s). The dashed black line indicates $y = x$, red dashed lines mark $T_{90} = 2$ s, and the orange dashed line marks $T_{90} = 4.2$ s obtained from the fourth Fermi Catalog (A. von Kienlin et al. 2020). Histograms along the top and right axes show the logarithmic distributions of Swift and Fermi T_{90} values, respectively, with fitted bimodal GMM (solid gold line) and individual short (dashed gold, lower mean) and long (dashed gold, higher mean) components. Vertical/horizontal lines indicate GRB 240825A's T_{90} values. The GMM fits reveal distinct short and long GRB populations, with probabilities of GRB 240825A being short calculated as 0.3% for Swift and 48.3 % for Fermi.

2.4.5. LBT Optical Observations

We observed the field of GRB 240825A with the twin Large Binocular Camera (LBCs) mounted on the LBT at Mt. Graham, AZ, USA, in the Sloan r' and z' bands at three epochs (Program: IT-2024B-023, PI: E. Maiorano): 2024 September 12 ($\sim$17.59 days postburst), 2024 September 28 ($\sim$33.70 days postburst), and 2024 November 9 ($\sim$75.52 days postburst), with varying exposure times ranging from 30 to 60 minutes per filter to optimize S/N ratios. LBT data were reduced using the standard pipeline (A. Fontana et al. 2014), which includes bias subtraction and flat-fielding, bad pixel and cosmic ray masking, astrometric calibration, and coaddition. We used `HOTPANTS`-based image subtraction to search for associated SN (see Section 4.4). We calibrated the LBT images against Pan-STARRS field stars and uncorrected for foreground Galactic extinction.

2.5. Radio Observations

As part of the multiwavelength coverage of GRB 240825A, radio observations from the Atacama Large Millimeter/submillimeter Array (97.5 GHz, T. Laskar et al. 2024), the Very Large Array (VLA; 8.6 GHz, C. Peña et al. 2024a), MeerKAT (1.3 GHz, C. Peña et al. 2024b), and the Australia Telescope Compact Array (multiple frequencies, A. Gulati et al. 2024) were included. These measurements were reported in public GCN circulars.

3. Results

3.1. Prompt Emission Temporal Characteristics

The duration of GRB 240825A depends strongly on the instrument, energy band, and treatment of the weak soft tail. In our Fermi-GBM analysis, the bright hard main pulse in the 50–300 keV band has $T_{90} = 3.968 \pm 0.091$ s (see Figure 3). This value should be interpreted as the duration of the main hard prompt-emission episode. Independent high-energy observations support a similarly short main-emission phase: C.-W. Wang et al. (2025) reported $T_{90} = 4.96^{+0.09}_{-0.13}$ s for GECAM-B in 40-6000 keV, $T_{90} = 2.15^{+0.25}_{-0.40}$ s for GECAM-C in 6–6000 keV, and $T_{90} = 1.90^{+0.15}_{-0.25}$ s for Insight-HXMT/HE in 30–1000 keV. These measurements indicate that the bright hard prompt episode was relatively short.

In contrast, Swift-BAT is more sensitive to softer emission and detects a weak tail following the main pulse. If this tail is included as a prompt emission, the BAT T_{90} duration becomes 57.20 ± 8.57 s. If the weak tail is instead interpreted as early afterglow and excluded, the BAT main-emission duration is much shorter, $T_{90} = 7.42 \pm 0.16$ s in the 15–350 keV band (C.-W. Wang et al. 2025). Additionally, Konus-Wind detected the total duration of the main emission of GRB 240825A of $\sim$2 s, followed by weaker emission and softer emission lasting until $\sim T_0 + 25$ s (D. Frederiks et al. 2024), and AstroSat CZTI measured the T_{90} duration of $6.2^{+0.9}_{-0.8}$ s (J. Joshi et al. 2024). These discrepancies highlight the limitations of using a fixed T_{90} criterion and point to the importance of probabilistic classification techniques—such as Gaussian mixture models (GMM)—to more robustly distinguish GRB populations across instruments (Z.-B. Zhang et al. 2016).

We analyzed the T_{90} durations[50] of GRBs jointly observed by BAT (15–350 keV) and GBM (50–300 keV) to investigate their classification into short and long categories (see Figure 4). Using a GMM, we fitted bimodal log-normal distributions to the $\log_{10}(T_{90})$ values for both instruments. The matched GRBs were classified into four categories: pure long

[50] https://user-web.icecube.wisc.edu/~grbweb_public/

(both $T_{90} > 2$ s), pure short (both $T_{90} \leqslant 2$ s), Fermi long–Swift short (Fermi > 2 s, Swift $\leqslant 2$ s), and Swift long–Fermi short (Swift > 2 s, Fermi $\leqslant 2$ s), represented by blue, red, green, and purple markers, respectively. For GRB 240825A, with Swift $T_{90} = 57.20 \pm 8.57$ s and Fermi $T_{90} = 3.968 \pm 0.091$ s, we calculated the probability of being a short GRB (S. B. Pandey et al. 2019) using the GMM posterior probabilities, finding a low probability (0.3 %) for Swift (consistent with a long GRB) and a high probability (48.3 %) for Fermi due to its proximity to the classification boundary. This analysis highlights the differences in T_{90} measurements between instruments, which arise not only from differences in energy sensitivity ranges (Swift: 15–350 keV; Fermi: 50–300 keV), but also from variations in effective area as a function of energy-both of which impact detection sensitivity.

3.2. Prompt Emission Empirical Correlations: Classical Classification of GRB 240825A

In this section, we classify GRB 240825A using standard prompt emission diagnostics, including the time-integrated peak energy-T_{90} duration (E_p–T_{90}) correlation, the MVT–T_{90} duration (t_{mvts}–T_{90}) relation, the Amati relation, and the lag–luminosity correlation.

3.2.1. E_p–T_{90}

The E_p–T_{90} (peak energy–duration) parameter space is a well-established diagnostic tool for distinguishing between merger and collapsar GRBs (R. D. Preece et al. 2000), particularly using Fermi-GBM observations (S. Poolakkil et al. 2021; R. Gupta et al. 2024b). To investigate the classification of GRB 240825A, we compiled a sample of GRBs from the Fermi-GBM catalog[51] and extracted their T_{90} and E_p ($404.81^{+9.02}_{-8.69}$ keV) values (peak energy from time-integrated spectral fits, Gupta et al. in preparation). We applied a two-component GMM in the log T_{90}–log E_p space to statistically separate the population into merger and collapsar GRBs. This probabilistic approach suggests a refined classification beyond the conventional hard threshold at $T_{90} = 2$ s, providing a likelihood estimate for each burst. GRB 240825A is located near the boundary between the two populations, with a probability of 71.6% of belonging to the collapsar GRB class. In Figure 5, we show the position of GRB 240825A on the E_p–T_{90} diagram, along with other GRBs associated with SNe and kilonovae, for context and comparison.

3.2.2. t_{mvts}–T_{90}

The t_{mvts} or MVT of a GRB is the shortest timescale over which coherent temporal variations in the light curve can be observed. When the GRB light curve exhibits multiple pulses, the MVT typically corresponds to the timescale of the shortest significant pulse. It has been shown that MVT, in combination with the burst duration (T_{90}), can effectively distinguish between collapsar and merger GRB populations (A. E. Camisasca et al. 2023). We compiled a sample of Fermi GRBs with t_{mvts} measurements from V. Z. Golkhou et al. (2015) and additional literature sources (P. Veres et al. 2023), and constructed the t_{mvts}–T_{90} distribution in log–log space. A two-component GMM was applied to this dataset to statistically separate the GRB population. GRB 240825A was found to have an MVT of 13.8 ± 1.6 ms utilizing GBM observations, as derived via the wavelet decomposition technique of V. Z. Golkhou et al. (2015). Its location on the t_{mvts}–T_{90} plane (see Figure 5, GRB 240825A along with other KN/SN connected GRBs) places it near the boundary of the merger and collapsar GRB populations, with a calculated merger GRB probability of 95.3%.

3.2.3. Amati Relation

The correlation between the intrinsic peak energy ($E_{p,i}$) and the isotropic-equivalent energy ($E_{\gamma,iso}$), known as the Amati relation, has long served as an empirical discriminator between collapsar and merger GRBs (L. Amati et al. 2002; Y.-P. Qin & Z.-F. Chen 2013). Collapsar GRBs tend to follow a tight correlation in the $E_{p,i}$–$E_{\gamma,iso}$ plane, while merger GRBs, including those with EE, typically fall above this track. To assess the nature of GRB 240825A, we compiled a sample of GRBs from the literature (P. Y. Minaev & A. S. Pozanenko 2020), including merger GRBs with and without EE, collapsar GRBs, and those with confirmed SN or KN associations (X. I. Wang et al. 2022; J. Yang et al. 2022; H. Sun et al. 2025). We then plotted these events in the $E_{p,i}$–$E_{\gamma,iso}$ plane and overlaid the best-fit Amati relations for collapsar and merger GRBs based on previous studies (P. Y. Minaev & A. S. Pozanenko 2020). GRB 240825A ($E_{\gamma,iso} = 1.56 \times 10^{53}$ erg), shown in Figure 5, lies within the 2σ scatter of the collapsar GRB correlation, overlapping with the region occupied by SN-associated long GRBs (SNe-long-duration GRBs). This placement suggests that GRB 240825A is more consistent with the collapsar GRB population in terms of energetics.

3.2.4. Lag–Luminosity Relation

The lag–luminosity relation, which connects the spectral lag (τ) and the isotropic peak luminosity ($L_{\gamma,iso}$), has been widely employed as a diagnostic to distinguish between merger and collapsar GRBs (J. P. Norris et al. 2000). Collapsar GRBs typically exhibit positive spectral lags (where higher-energy photons arrive earlier than lower-energy ones) and follow a strong anticorrelation between lag and luminosity (J. P. Norris 2002). In contrast, merger GRBs often show negligible or even negative lags, deviating from the collapsar GRB track in this parameter space (T. N. Ukwatta et al. 2010; M. G. Bernardini et al. 2015). We collected a sample of GRBs with measured lags and luminosities, including both positive and negative lag populations for merger and collapsar GRBs (T. N. Ukwatta et al. 2010; M. G. Bernardini et al. 2015; M. D. Caballero-García et al. 2023).

We calculated the spectral lag for GRB 240825A using the cross-correlation function (CCF) between the 15–25 keV and 50–100 keV light curves from the Swift-BAT, focusing on the time interval from 0.67 to 7.58 s postburst. Employing a robust CCF computation with `numpy.correlate` and Monte Carlo error estimation, we fitted the CCF peak with an asymmetric Gaussian model via Markov Chain Monte Carlo (MCMC) sampling, yielding a spectral lag of $\sim 0.014 \pm 0.009$ s (68% confidence), indicating that the softer 15–25 keV band lags the harder 50–100 keV band. To contextualize GRB 240825A within the lag–luminosity relation, we estimated its isotropic peak luminosity (L_{iso}) utilizing a peak flux derived from GBM data (R. Gupta et al. 2026, in preparation). As shown in Figure 5, GRB 240825A (pink star) satisfies the

[51] https://heasarc.gsfc.nasa.gov/W3Browse/fermi/fermigbrst.html

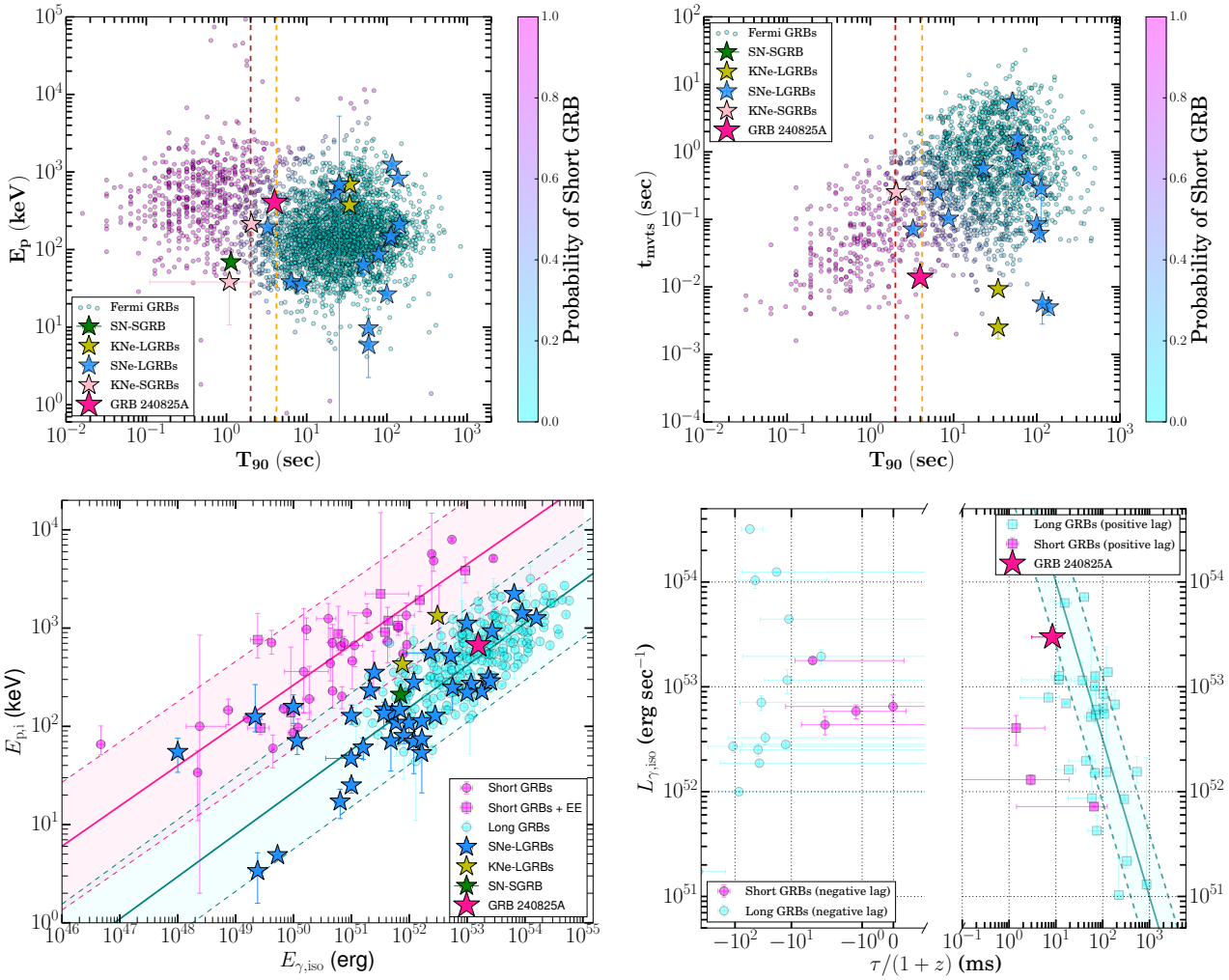


Figure 5. Prompt emission empirical correlations: Top-left: scatter plot of peak energy (E_p) vs. T_{90} duration for a sample of GRBs detected by Fermi-GBM. Top-right: log–log scatter plot of MVT timescale (in seconds) vs. T_{90} duration (in seconds) for GRBs detected by Fermi-GBM. Red dashed lines mark $T_{90} = 2$ s, and the orange dashed line marks $T_{90} = 4.2$ s, respectively. Bottom-left: log–log scatter plot of peak energy (E_p) vs. isotropic-equivalent energy ($E_{\gamma,iso}$) for GRBs obtained from P. Y. Minaev & A. S. Pozanenko (2020). The dashed lines represent the Amati relation for collapsar (cyan) and merger (pink) GRBs (P. Y. Minaev & A. S. Pozanenko 2020). GRB 240825A, with an estimated rest-frame $E_p \approx$ 671.57 keV and $E_{\gamma,iso} \approx 1.6 \times 10^{53}$ erg, falls within the collapsar GRB cluster, indicating its classification as a collapsar GRB. Bottom-right: GRB 240825A in the lag–luminosity plane $\log(\tau)$ vs. $\log(L_{iso})$, compared to a sample of Swift-BAT GRBs, marginally following the long-duration GRB lag (rest frame)–luminosity relation (T. N. Ukwatta et al. 2010).

collapsar GRB lag–luminosity relation, with a rest-frame lag of $\tau/(1+z) \approx 8.44$ ms and $L_{\gamma,iso} \approx 2.98 \times 10^{53}$ erg s^{-1}.

3.3. Fermi and Atmosphere–Space Interactions Monitor Timing Analysis of GRB 240825A

We searched for quasiperiodic oscillations (QPOs; M. D. Caballero-García et al. 2025) in the prompt light curves using power density spectra (PDS) from the Atmosphere–Space Interactions Monitor (ASIM) High Energy Detector (HED; T. Neubert et al. 2019) and Fermi-GBM (see Figure A1 and Table A2 in the Appendix). We noticed low-significance peaks at around 6 and 20 Hz, with single-trial significance of 0.3, 1.3σ for ASIM-HED and with an F-test probability of 0.56, 0.60 for Fermi-GBM. Given these low significance levels, we consider the QPO evidence inconclusive and do not further use it in the progenitor classification.

3.4. Afterglow Temporal and Spectral Evolution

We conducted the analysis of the optical r-band light curve of GRB 240825A using data from Y. Cheng et al. (2025), L. Izzo & D. B. Malesani (2024), SVOM/C-GFTTeam et al. (2024), A. Martin-Carrillo et al. (2024), R. Brivio et al. (2024), E. Le Floc'h et al. (2024), B. T. Wang et al. (2024), and F. D. Romanov (2024), focusing on the first 10^5 s to avoid contamination from the host galaxy (see Figure 6). The optical light curve was fitted using a broken power-law function (see Table 2). The observed transition from a steeper decay ($\alpha_{O1} = -1.60$) to a shallower decay ($\alpha_{O2} = -0.94$) is consistent with a transition from the reverse shock-dominated phase to the forward shock-dominated phase (e.g., R. Sari & T. Piran 1999). Given the prompt duration $T_{90} = 3.96$ s (Fermi-GBM), the break time at $\sim$426 s satisfies the condition $t_{dec} \gg T_{90}$, indicating the thin-shell case (C. Wu et al. 2025). In this regime, the reverse shock is Newtonian, and the temporal decay of optical emission (in the slow-cooling regime and for $\nu > \nu_m^{RS}$) follows $\alpha = -\frac{27p+7}{35}$ (B. Zhang & S. Kobayashi 2005; R. Gupta et al. 2026). Solving for p, we find $p \approx 1.81$, a physically reasonable value for GRB ejecta and consistent with other GRB reverse shock studies (R. Gupta et al. 2021). On the other hand, the shallow postbreak decay index ($\alpha_{O2} = -0.94$) is consistent

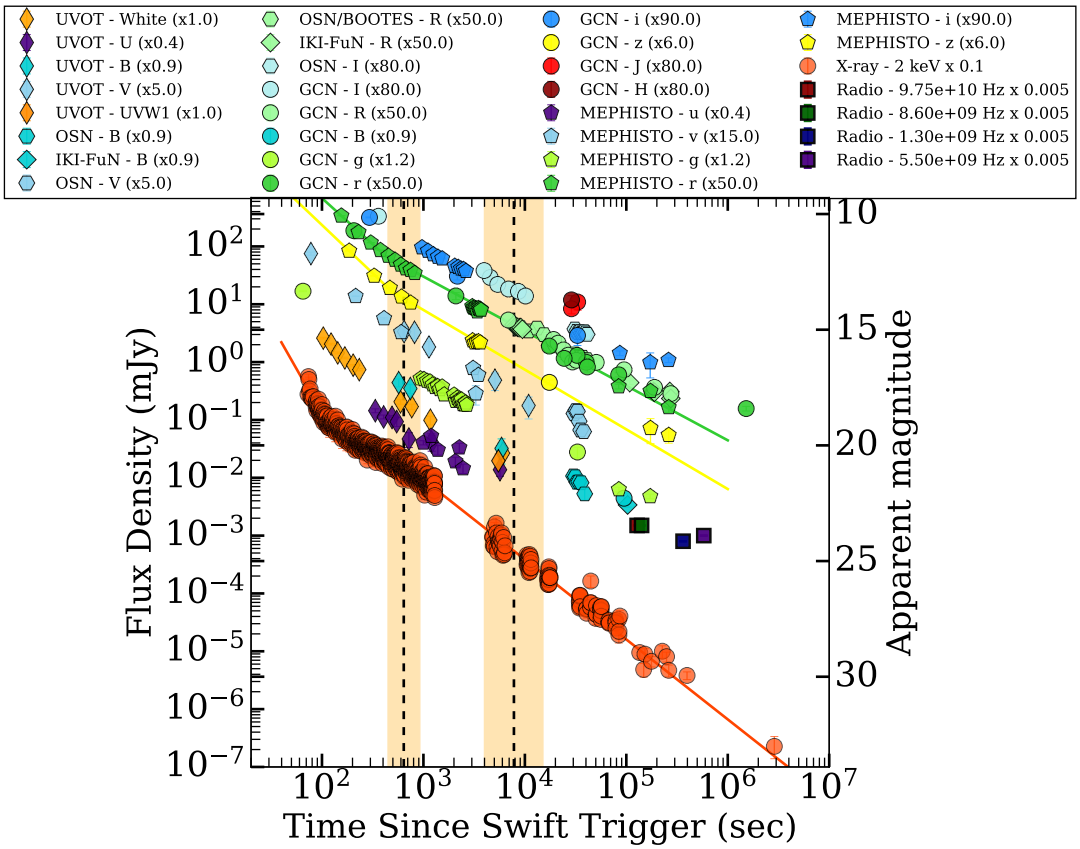


Figure 6. Multiwavelength light curves of the GRB 240825A afterglow. Solid lines in different colors represent best-fit power-law or broken power-law models applied to the observed data points. Optical data have been corrected for Galactic extinction. Vertical orange shaded bands mark the time intervals used for constructing the SEDs, with vertical black dashed lines indicating the central times of the SEDs.

Table 2
Summary of the Temporal Fit Parameters for the Optical and X-Ray Afterglow Light Curves of GRB 240825A

Band	Model	Temporal Index	Break Time (s)
Optical	Broken power law	$\alpha_{O1} = -1.60 \pm 0.01$	$t_{\rm opt} = 425.95 \pm 6.70$
Optical	⋯	$\alpha_{O2} = -0.94 \pm 0.01$	⋯
X-ray, 2 keV	Double broken power law	$\alpha_{X1} = -3.11 \pm 0.25$	$t_{X1} = 115.94 \pm 2.42$
X-ray, 2 keV	⋯	$\alpha_{X2} = -0.97 \pm 0.02$	⋯
X-ray, 2 keV	⋯	$\alpha_{X3} = -1.38 \pm 0.02$	$t_{X2} = 836.65 \pm 40.10$

with the expected range for forward shock emission in a constant-density interstellar medium, where the temporal decay index is related to the electron energy distribution index, p, via $\alpha = (3p - 3)/4$ for a slow-cooling regime, i.e., $\nu_{\rm opt} < \nu_{\rm c} < \nu_{\rm X-ray}$ or $\nu_{\rm opt} < \nu_{\rm X-ray} < \nu_{\rm c}$ (R. Sari et al. 1998). Assuming $\alpha_{O2} = -0.94$, this implies $p \approx 2.25$ (C. Wu et al. 2025).

The X-ray afterglow light curve at 2 keV was best described by a double broken power-law model (see Table 2). We also conducted a spectral analysis of the XRT data during the early steep decay phase ($t < 118$ s). The spectrum was modeled with a power-law function, yielding an X-ray spectral index of $\beta = -1.28^{+0.10}_{-0.09}$. This steep decay phase is consistent with high-latitude emission, commonly interpreted as the tail of the prompt GRB emission, where photons from off-axis regions arrive at the observer with a delay due to geometric effects (e.g., P. Kumar & A. Panaitescu 2000). For nonthermal emission described by a single power-law, the temporal decay index is theoretically related to the spectral index by the relation $\alpha = -2 + \beta$. Given the measured spectral index $\beta = -1.28^{+0.10}_{-0.09}$, the expected temporal decay index is approximately $-3.28^{+0.10}_{-0.09}$, which is in agreement with the observed value of $\alpha_{X1} = -3.11 \pm 0.25$.

We further generated two joint spectral energy distributions (SEDs) using contemporaneous UVOT and XRT data, centered at T_0 +640 s (SED 1) and T_0 +7800 s (SED 2). We followed the methodology described by P. Schady et al. (2007, 2010) to construct the SEDs, and both SEDs were analyzed using XSPEC (version 12.12.0), following the procedures in P. Schady et al. (2007, 2010). We tested two continuum models: a simple power

law (POW) and a broken power law (BKP). For the BKP model, the high-energy spectral index was fixed according to $\beta_2 = \beta + 0.5$, as expected for a synchrotron cooling transition. Each model incorporated two dust and gas components to account for Galactic and host galaxy extinction and photoelectric absorption, using the `phabs`, `zphabs`, and `zdust` models in `XSPEC`. The Galactic components were fixed to the reddening values from D. J. Schlegel et al. (1998) and column density from P. M. W. Kalberla et al. (2005). For the host galaxy, we tested three extinction laws: Small Magellanic Cloud (SMC), Large Magellanic Cloud (LMC), and Milky Way (MW) extinction laws. To reduce the degeneracy between intrinsic low-energy spectral curvature and photoelectric absorption, we did not allow the host galaxy absorbing column to vary independently between the two epochs. We first determined the host galaxy column density from the XRT-only spectrum at the epoch corresponding to SED 1, approximately $T_0 + 640$ s. The XRT-only fit gave $N_{\rm H,z} = 8.68 \times 10^{22}\,{\rm cm}^{-2}$. We then fixed $N_{\rm H,z}$ at this value in all broadband fits to both SEDs and for all continuum and extinction models. Our analysis therefore assumes a time-independent line-of-sight absorbing column.

The fits were evaluated using the reduced chi-squared relative to degrees of freedom (χ^2/dof), and the null hypothesis probability. For both SEDs, BKP provided the best fit (see Table 3 and Figure 7). For SED 1, the single power-law fits are statistically unacceptable for all three extinction laws, with null hypothesis probabilities of order 10^{-8}. In contrast, the broken power-law fits are acceptable, with null hypothesis probabilities ranging from 0.21 to 0.24. The improvement is substantial for all three extinction laws. For example, for the LMC extinction law, the fit statistic improves from $\chi^2/{\rm dof} = 636.96/459$ for the single power law to $\chi^2/{\rm dof} = 482.00/458$ for the BKP. At the second epoch, the BKP also gives a lower χ^2 than the corresponding single power-law model for all three extinction laws. The best-fitting model among those tested for SED 2 (higher number of UVOT filters) is the BKP with LMC extinction, for which $\chi^2/{\rm dof} = 44.82/55$ and the null hypothesis probability is 0.835. The corresponding single power law LMC fit gives $\chi^2/{\rm dof} = 70.21/56$. Adopting the LMC extinction law consistently at both epochs, the BKP parameters are $\beta_1 = 1.29 \pm 0.02$, 7D17D1$E(B-V) = 0.27 \pm 0.02$ mag, 7D17D1 $E_{\rm bk} = 2.07 \pm 0.10$ keV for SED 1, and $\beta_1 = 1.37 \pm 0.04$, 7D17D1 $E(B-V) = 0.35 \pm 0.03$ mag, and 7D17D1 $E_{\rm bk} = 2.15 \pm 0.28$ keV for SED 2.

We emphasize that the BKP model is a phenomenological description of the broadband curvature. A physical synchrotron spectrum is expected to exhibit a smooth transition around the cooling frequency rather than an infinitesimally sharp break, and this curvature may extend over a broad frequency interval (J. Granot & R. Sari 2002; H. J. van Eerten & R. A. M. J. Wijers 2009; Z. L. Uhm & B. Zhang 2014). Consequently, the fitted value of $E_{\rm bk}$ can depend on the assumed continuum and extinction law and should not necessarily be identified with a sharply defined synchrotron cooling frequency. This qualification is also supported by the temporal behavior. At approximately $T_0 + 640$ s, the postbreak optical and contemporaneous X-ray temporal indices are similar, $\alpha_{\rm O,2} = -0.94 \pm 0.01$ and $\alpha_{\rm X,2} = -0.97 \pm 0.02$. A cooling break cleanly separating the optical and X-ray bands would generally predict different temporal indices in the two bands. Furthermore, if the fitted $E_{\rm bk} \sim 2$ keV were identified directly with the synchrotron cooling frequency, the expected

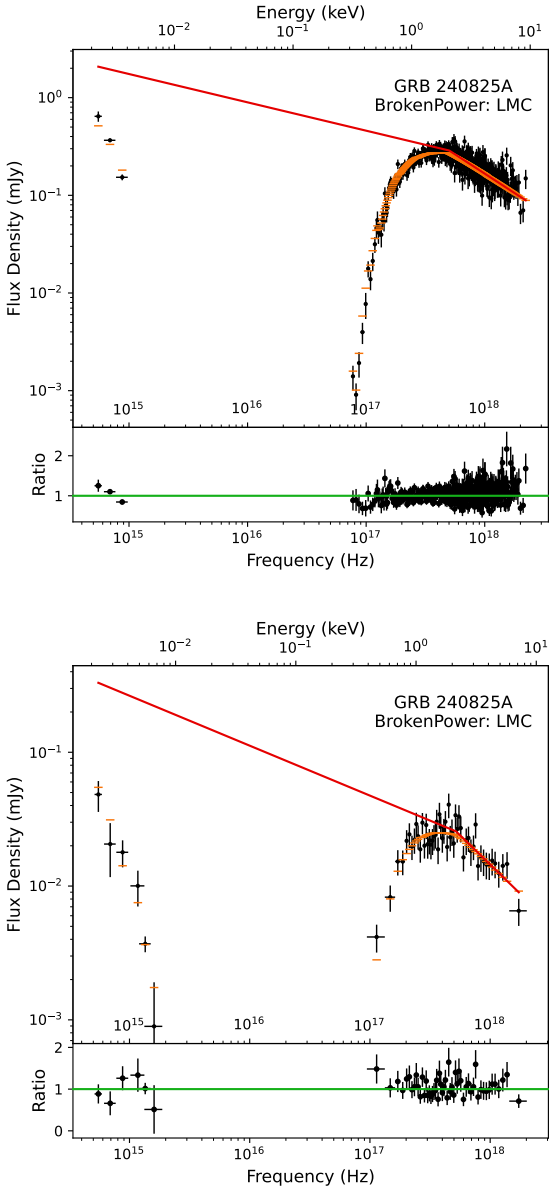


Figure 7. Combined X-ray and UV/optical SEDs for GRB 240825A. Top panel: SED 1, centered at T_0 +640 s, constructed from UVOT data in the *u*, *b*, and *v* filter observations and contemporaneous XRT data. Bottom panel: SED 2, centered at $T_0 + 7800$ s, constructed using UVOT data in the *u*, *b*, *v*, *uvw*1, *uvw*2, and *uvm*2 filter observations and XRT data. Both SEDs were optimally fitted with a broken power-law model, with the LMC extinction law providing the best fit. The host galaxy absorbing column density ($N_{\rm H,z}$) was fixed at 8.68×10^{22} cm^{-2} in both SEDs. Observed and model data points are shown in black and orange, respectively. The solid red line represents the best-fit model corrected for absorption and extinction. The lower subpanel in each figure displays the data-to-model ratio, demonstrating the quality of the fit across the energy range. The broken power law provides a phenomenological description of the broadband curvature; its fitted break energy should not necessarily be interpreted as a sharply defined synchrotron cooling frequency.

temporal evolution would not be reproduced. In a constant-density medium, $\nu_c \propto t^{-1/2}$, so the break should move to lower energy by a factor of $\sim(7800/640)^{-1/2} \approx 0.29$ between the two SED epochs. In a wind-like medium, the expected evolution is in the opposite direction, $\nu_c \propto t^{1/2}$, and an increase by a comparable factor would be expected. Instead, the fitted LMC break energies remain approximately constant within the uncertainties: $E_{\rm bk} = 2.07 \pm 0.10$ keV and $E_{\rm bk} = 2.15 \pm 0.28$ keV. We therefore interpret $E_{\rm bk}$ as an

Table 3
Results of Simultaneous UV/optical and X-ray Spectral Fits for GRB 240825A Using MW, LMC, and SMC Extinction Laws with POW or BKP Continuum Models

SED	Model	Dust	β	$E(B-V)$ (mag)	E_{bk} (keV)	χ^2 (dof)	Null Hypothesis Probability
SED 1 (T_0 +640 s)							
640 s	POW	MW	1.52 ± 0.01	0.46 ± 0.01	⋯	642.23 (459)	3.12e-08
640 s	POW	LMC	1.52 ± 0.01	0.45 ± 0.01	⋯	636.96 (459)	6.75e-08
640 s	POW	SMC	1.52 ± 0.01	0.47 ± 0.01	⋯	637.65 (459)	6.12e-08
640 s	BKP	MW	1.29 ± 0.02	0.26 ± 0.02	2.06 ± 0.10	479.35 (458)	2.37e-01
640 s	BKP	LMC	1.29 ± 0.02	0.27 ± 0.02	2.07 ± 0.10	482.00 (458)	2.11e-01
640 s	BKP	SMC	1.29 ± 0.02	0.26 ± 0.02	2.06 ± 0.10	480.31 (458)	2.27e-01
SED 2 (T_0 +7800 s)							
7800s	POW	MW	1.60 ± 0.04	0.62 ± 0.04	⋯	59.32 (56)	3.56e-01
7800s	POW	LMC	1.49 ± 0.03	0.40 ± 0.03	⋯	70.21 (56)	9.59e-02
7800s	POW	SMC	1.41 ± 0.03	0.31 ± 0.03	⋯	90.19 (56)	2.56e-03
7800s	BKP	MW	1.50 ± 0.07	0.56 ± 0.06	2.79 ± 0.62	50.48 (55)	6.48e-01
7800s	BKP	LMC	1.37 ± 0.04	0.35 ± 0.03	2.15 ± 0.28	44.82 (55)	8.35e-01
7800s	BKP	SMC	1.28 ± 0.04	0.24 ± 0.02	1.81 ± 0.30	48.12 (55)	7.33e-01

Note. For the BKP, the high-energy spectral index was fixed according to $\beta_2 = \beta + 0.5$. Columns list the low-energy spectral index (β), color excess ($E(B-V)$), break energy (E_{bk}) for broken power-law models, fit statistic χ^2, degrees of freedom (dof), and null hypothesis probability. In every fit, host galaxy absorbing column density ($N_{\rm H,z}$) was fixed at 8.68×10^{22} cm^{-2}, as determined from the XRT-only spectrum at the epoch corresponding to SED 1, approximately T_0 +640 s. Thus, the fits assume a time-independent host-galaxy absorbing column density.

empirical measure of the broadband curvature sampled primarily by the XRT band, rather than as a robust direct measurement of ν_c. Under this interpretation, the cooling frequency is likely close to or above the X-ray band, but the present data do not allow us to determine its exact location robustly.

The broadband afterglow is broadly consistent with synchrotron emission, but no single standard closure relation simultaneously explains all temporal and spectral indices. This tension may indicate a complex afterglow evolution, potentially driven by a two-component jet model (e.g., a narrow core and wider cocoon), a wavelength-dependent model, a transition in the external medium density profile (e.g., from wind to ISM), evolving microphysical parameters, or a structured outflow. Alternatively, the circumburst environment may follow a nontrivial density profile, parameterized as $\rho \propto r^{-k}$ with $0 \leqslant k \leqslant 2$, which has been shown to affect the temporal and spectral indices (H. Gao et al. 2013). Further multi-wavelength observations, including radio and high-energy data, are essential to refine these models and elucidate the physical processes governing the afterglow of GRB 240825A.

3.5. Host Galaxy Properties

Host galaxy properties provide crucial context for distinguishing between collapsar and merger GRBs, offering insights into their progenitor systems (A. S. Fruchter et al. 2006; S. Savaglio et al. 2009; W. Fong et al. 2013; E. Berger 2014). In our analysis, we utilize the host galaxy properties to probe the likely progenitor and classify the physical origin of GRB 240825A.

3.5.1. Host SED Analysis

We conducted a comprehensive SED analysis of the host galaxy of GRB 240825A using the Prospector (see Figure 8). The SED was constructed using the GTC spectrum and broadband photometry spanning optical to mid-infrared wavelengths, including deep imaging from the 10.4 m GTC in the g, r, i, z, J, H, and K bands, and archival data from the DESI Legacy Surveys in the W1, W2, and W3 bands. Data

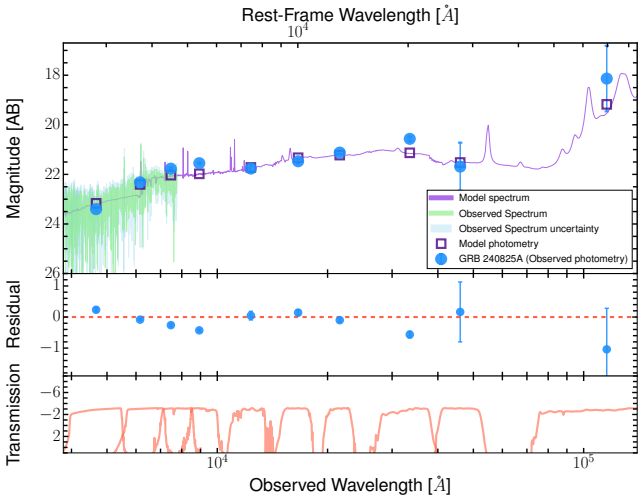


Figure 8. Best-fit SED model for the host galaxy of GRB 240825A using `Prospector`. The sky-blue points represent observed photometry from 10.4 m GTC and DESI Legacy Surveys in the g, r, i, z, J, H, K, W1, W2, and W3 bands. Residuals between the observed and modeled fluxes are shown in the middle panel, with a dashed line marking the residuals equal to zero. The transmission of each filter is shown in the lower panel.

were corrected for galactic extinction using the E. F. Schlafly & D. P. Finkbeiner (2011) dust maps, while dust attenuation was fixed to the afterglow-derived line-of-sight value within Prospector. We employed the `parametric_sfh` model[52] in Prospector, assuming a delayed-τ star formation history (SFR(t) $\propto (t/\tau^2)e^{-t/\tau}$), and sampled the parameter space using MCMC methods. Key parameters included stellar mass ($M_\star$), metallicity (Z), galaxy age ($t_{\rm age}$), and the e-folding time (τ). The corner plot (see Figure A2 of the Appendix) displays posterior distributions for parameters. The best-fit model yields a stellar mass of $\log(M_\star/M_\odot) \approx 10.01$ and a star formation timescale of $\tau \approx 0.62$ Gyr. The SFR, derived from

[52] https://prospect.readthedocs.io/en/latest/sfhs.html

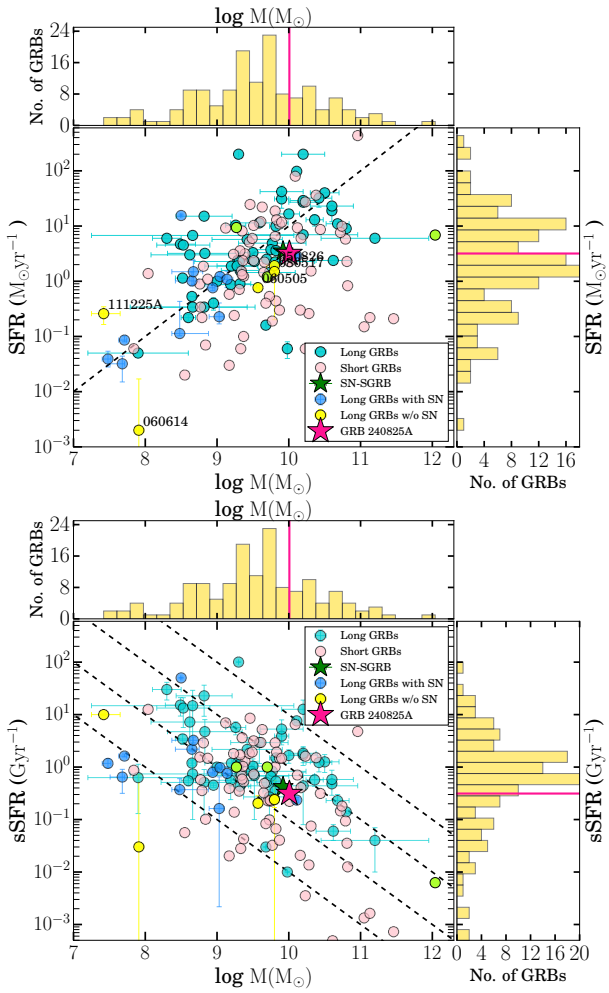


Figure 9. This figure illustrates the host galaxy properties of GRB 240825A compared to collapsar (depicted with cyan circles) and merger (depicted with pink circles) GRBs taken from S. Savaglio et al. (2006, 2009), K. Taggart & D. A. Perley (2021), A. E. Nugent et al. (2022), and R. Gupta et al. (2022b). Top panel: stellar mass (log $M/M_{\odot}$) vs. SFR (SFR/$M_{\odot}$ yr^{-1}). Histograms of stellar mass and SFR are shown along the top X-axis and right Y-axis, respectively. A dashed black line denotes a specific star formation rate of 1 Gyr^{-1}, representing the main sequence of star-forming galaxies. Bottom panel: stellar mass vs. sSFR (sSFR yr^{-1}), with histograms of stellar mass and sSFR along the top X-axis and right Y-axis, respectively. In both panels, GRB 240825A's host galaxy is highlighted with a pink star, and its position in the histograms is marked by vertical pink lines. Dashed black lines denote sSFRs of 0.1, 1, 10, and 100 $M_{\odot}$ yr^{-1}.

the model, is approximately 3.18 $M_{\odot}$ yr^{-1}, consistent with a star formation history for a massive galaxy.

3.5.2. Comparative Analysis of GRB 240825A Host Galaxy Properties with Collapsar and Merger GRB Hosts

Using the Prospector tool, we derived the stellar mass, SFR, and specific star formation rate (sSFR) of the host galaxy of GRB 240825A to contextualize its properties relative to other GRB hosts and infer its progenitor environment. The host's parameters (see Figure A2 of the Appendix) are consistent with a moderately star-forming dusty galaxy at its redshift ($z = 0.659$). GRB 240825A's host is typical of the main sequence of star-forming galaxies in the log SFR versus log $M/M_{\odot}$ and log sSFR versus log $M/M_{\odot}$ planes (see Figure 9). These properties—a relatively massive host, subsolar metallicity, and ongoing star formation—are consistent with typical hosts of long-duration GRBs (S. Savaglio et al. 2009; R. Gupta et al. 2022b).

3.5.3. Host Offset and Progenitor Implications

The projected physical offset between a GRB afterglow and its host galaxy center provides key insights into the nature of its progenitor system. Collapsar GRBs, believed to originate from the collapse of massive stars, are typically found near the star-forming regions of their hosts and thus exhibit smaller offsets. In contrast, merger GRBs, which are thought to result from compact object mergers, often show larger offsets due to natal kicks and long inspiral times (e.g., W. Fong et al. 2010; E. Berger 2014). For GRB 240825A, we derive a projected offset of 4.54 kpc based on the angular separation ($0\farcs64$) between the VLA-detected afterglow position (R.A.: 22:58:17.27, decl.: +01:01:36.78, C. Peña et al. 2024a) and the host galaxy centroid (R.A.: 22:58:17.23, decl.: +01:01:36.48). In the context of known GRB populations (J. S. Bloom et al. 2002; P. K. Blanchard et al. 2016; W.-f. Fong et al. 2022; B. O'Connor et al. 2022), this offset lies between the typical ranges for merger and collapsar GRBs. Specifically, collapsar GRBs have a mean (median) offset of 2.43 kpc (1.45 kpc), while merger GRBs exhibit significantly larger mean (median) values of 13.84 kpc (7.82 kpc). Figure 10 shows the offset distribution for both GRB classes and the cumulative distribution comparison. The offset of GRB 240825A is more consistent with the upper tail of collapsar GRB offsets, suggesting a probable massive star origin.

4. Discussion

4.1. Rest-frame Energetics: $E_{\gamma,iso}$ and $E_{p,i}$

Understanding the redshift evolution of prompt emission properties such as the isotropic-equivalent gamma-ray energy ($E_{\gamma,\rm iso}$) and rest-frame peak energy ($E_{\rm p,i}$) is critical for classifying GRBs and probing their progenitor systems. Collapsar GRBs, associated with collapsars, typically exhibit higher $E_{\gamma,\rm iso}$ and lower $E_{\rm p,i}$ values over a broad redshift range, while merger GRBs, often originating from compact binary mergers, tend to occupy a distinct region in this parameter space with lower energetics and higher spectral hardness. We compared the location of GRB 240825A in the $E_{\gamma,\rm iso}$ versus $(1+z)$ and $E_{\rm p,i}$ versus $(1+z)$ planes against a well-classified GRB population from P. Y. Minaev & A. S. Pozanenko (2020), H. Sun et al. (2025), and J. Yang et al. (2022). As shown in Figure 11, GRB 240825A (pink star) appears consistent with typical collapsar GRBs.

4.2. GRB 240825A: New Classification Schemes and Possible Progenitor

In recent times, some authors have proposed physically motivated classifications of GRBs to complement the traditional duration-based scheme. For example, P. Y. Minaev & A. S. Pozanenko (2020) introduced a robust classification scheme based on two parameters: energy hardness (EH) and energy-hardness-duration (EHD). These parameters provide a valuable diagnostic tool for GRB classification, especially when traditional duration- or spectral-based criteria prove ambiguous. In the EH–EHD parameter space, collapsar GRBs (Type II) tend to occupy regions with low EH–EHD, while merger GRBs (Type I) cluster at higher values of both

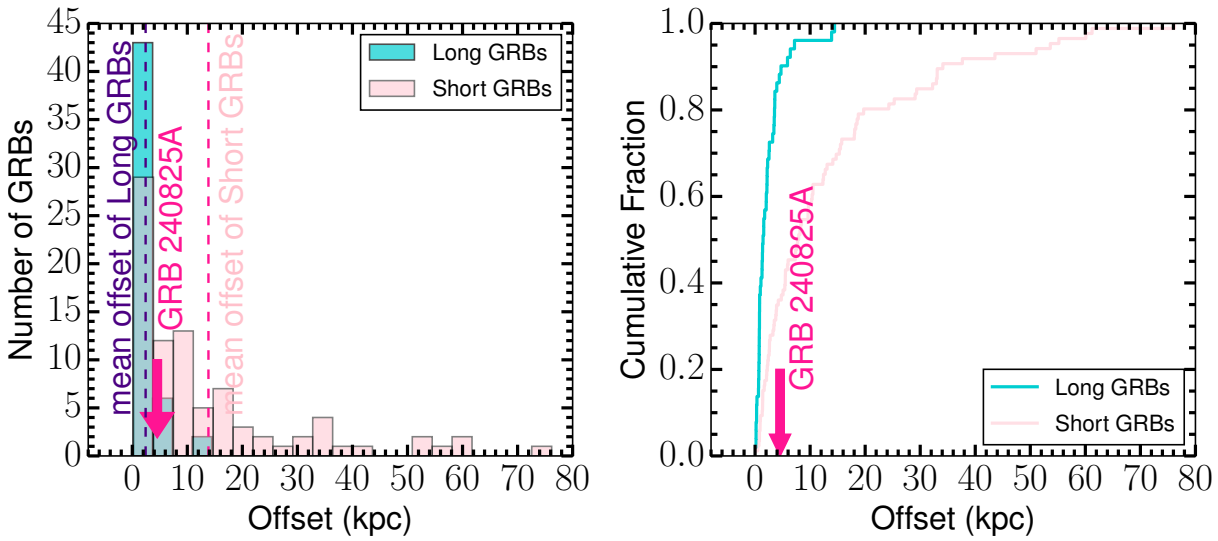


Figure 10. Left panel: histogram of physical offsets (in kiloparsecs) for collapsar GRBs (cyan) and merger GRBs (light pink), with the mean offset of GRB 240825A (4.54 kpc) marked by a pink arrow. The mean offsets are 2.426 kpc for collapsar GRBs and 13.838 kpc for merger GRBs, with medians of 1.451 kpc and 7.820 kpc, respectively. Right panel: Cumulative fraction of offsets for collapsar GRBs (cyan) and merger GRBs (light pink), with the position of GRB 240825A (4.54 kpc) indicated by a pink arrow. The offset of GRB 240825A, derived from the host position (R.A. 22:58:17.23, decl. +01:01:36.48) and VLA position (R.A. 22:58:17.27, Decl. +01:01:36.78, C. Peña et al. 2024a) at ($z = 0.659$), suggests an intermediate location between typical collapsar and merger GRB populations, hinting at a potential off-axis massive star progenitor scenario.

parameters. In Figure 12, we compare GRB 240825A against this framework. Our analysis places the burst in a region overlapping with Type II GRBs (see Figure 12). We also analyzed GRB 211211A and GRB 230307A (long merger events, J. Yang et al. 2022; H. Sun et al. 2025) following the same parameter spaces and noted that GRB 211211A is consistent with Type II GRBs; however, for GRB 230307A, the EH parameter suggests that the burst possibly belongs to Type I GRBs.

An important tool for understanding the physical origin of GRBs lies in the classification based on their prompt emission properties. However, the traditional scheme does not always correlate well with the underlying progenitor systems, namely collapsars (Type II) and compact object mergers (Type I). To address this, H.-J. Lü et al. (2010) introduced a new phenomenological classification method based on the parameter $\varepsilon \equiv E_{\gamma,\mathrm{iso},52}/E_{p,z,2}^{5/3}$, where $E_{\gamma,\mathrm{iso},52}$ is the isotropic gamma-ray energy in units of 10^{52} erg and $E_{p,z,2}$ is the rest-frame spectral peak energy in units of 100 keV. This parameter shows a clear bimodal distribution with a division at $\varepsilon \sim 0.03$, effectively distinguishing Type I and Type II GRBs. In Figure 13, we plot GRB 240825A in the $\log T_{90,i}$–$\log \varepsilon$ plane, alongside other GRBs (obtained from P. Y. Minaev & A. S. Pozanenko 2020; J. Yang et al. 2022; H. Sun et al. 2025) classified using this scheme. GRB 240825A lies in the high-ε, but short-duration region, clustering with classical Type I bursts ($T_{90,i}$) and Type II GRBs (ε), supporting a hybrid origin (merger from $T_{90,i}$ and collapsar from ε).

4.3. ML-based Progenitor Classification of GRB 240825A

Recent ML approaches provide useful, but not definitive, ways to compare GRBs in multidimensional prompt-emission parameter spaces. One such technique is the t-distributed stochastic neighbor embedding (t-SNE), which performs unsupervised dimensionality reduction on the high-dimensional prompt emission light curves to reveal intrinsic clustering in a lower-dimensional space (C. K. Jespersen et al. 2020). This method, applied to the full Swift-GRB catalog, results in an unambiguous separation into two well-defined groups that broadly correspond to collapsar and merger GRBs, respectively. The classification is purely empirical and based on the global similarity of light curves, retaining rich temporal and spectral structure. We caution that this map should not be interpreted as a clean physical separation between collapsar and merger progenitors. As shown in Figure 14, the t-SNE projection most clearly separates the population of classical short GRBs from the broader long-duration population. Several hybrid or unusual events, including short GRBs with EE and long GRBs with KN signatures, overlap with standard long GRBs. This indicates that duration and broad light-curve morphology remain important drivers of the embedding. Figure 14 presents the position of GRB 240825A on the t-SNE map along with a sample of Swift-detected GRBs. The burst is consistent with Type-L (long) GRBs.

Furthermore, P. Nuessle et al. (2024) demonstrated that ML methods can classify GRB progenitors using prompt emission observables, moving beyond simplistic duration-based schemes. In particular, the ratio of the spectral peak energy (E_p) to fluence (S) in the 10–1000 keV band, plotted against the burst duration (T_{90}), serves as a physically motivated proxy to distinguish progenitor types, as collapsars and compact object mergers tend to populate different regions in this plane. This methodology was adopted in a probabilistic framework using a support vector machine (SVM) with a radial basis function kernel, trained on a sample of GRBs with known progenitor associations. We applied this classifier to GRB 240825A and obtained a probability of ∼76% for a collapsar origin and ∼24% for a merger origin. The fourth Fermi Catalog suggested a boundary of 4.2 s for classifying GRBs (A. von Kienlin et al. 2020). We noted that GRB 240825A has a duration slightly below this Fermi-GBM threshold. Following the classification scheme proposed by P. Nuessle et al. (2024), GRB 240825A would likely be considered a short collapsar similar to GRB 200826A (see Figure 15, T. Ahumada et al. 2021).

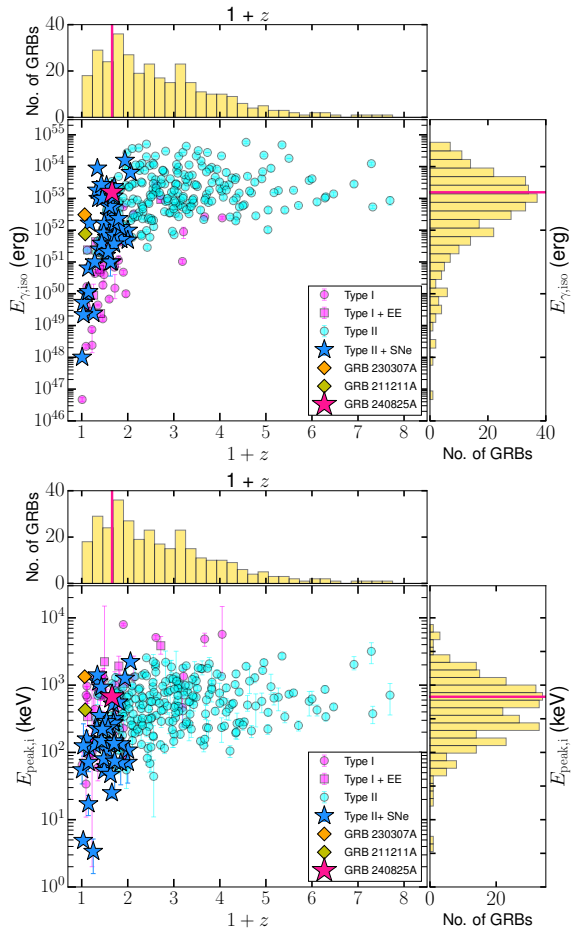


Figure 11. Top panel: isotropic-equivalent energy $E_{\gamma,iso}$ plotted against redshift for a sample of classified GRBs from P. Y. Minaev & A. S. Pozanenko (2020). GRB 240825A (pink star) is shown alongside GRB 211211A and GRB 230307A for comparison. Merger GRBs (Type I), merger GRBs with EE (Type I+EE), collapsar GRBs (Type II), and collapsar GRBs with confirmed SNe (Type II+SNe) are color coded. Bottom panel: rest-frame spectral peak energy $E_{p,i}$ as a function of redshift, with the same GRB sample. In these planes, GRB 240825A (pink star) appears consistent with typical collapsar GRBs.

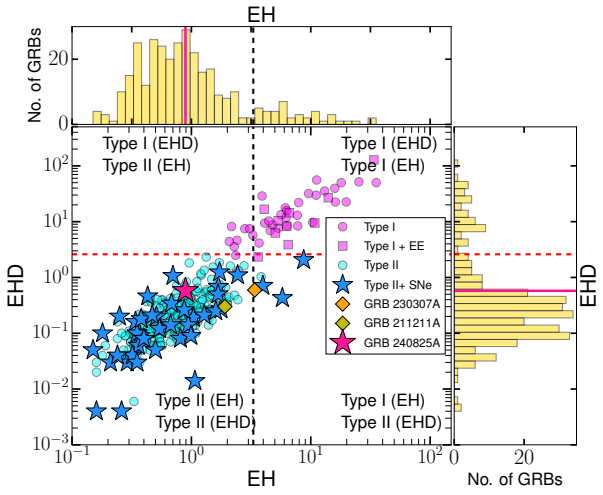


Figure 12. EHD vs. EH distribution of gamma-ray bursts from P. Y. Minaev & A. S. Pozanenko (2020), showing the distinction between Type I, Type II, those with EE (Type I+EE), and Type II+SNe. GRB 240825A (pink star) is shown alongside GRB 211211A and GRB 230307A for comparison. GRB 240825A lies close to the classical Type II GRB region. The vertical black and red horizontal dashed lines show EHD= EH, respectively.

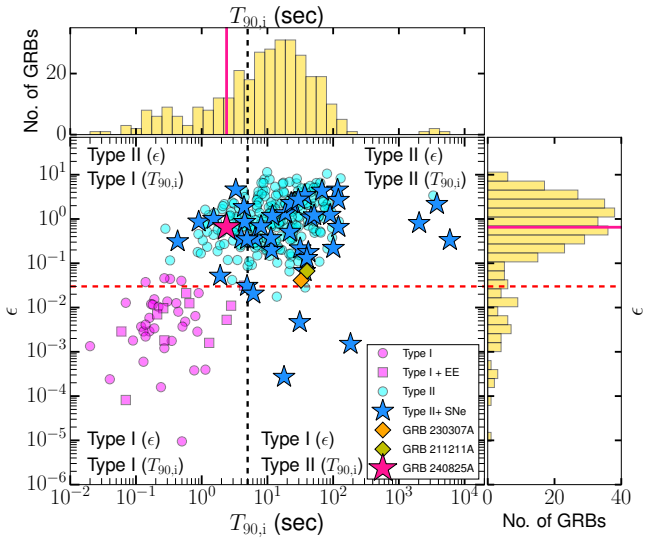


Figure 13. Rest-frame duration $T_{90,i}$ vs. ε for GRB 240825A (pink star), compared with the population of GRBs classified using the ε method (H.-J. Lü et al. 2010). The plot shows distinct regions occupied by Type I (merger origin) and Type II (collapsar origin) GRBs, with special populations such as Type I with EE and Type II associated with SNe (II+SNe) indicated. GRB 240825A falls within the high-ε, but short-duration region, clustering with classical Type I bursts ($T_{90,i}$) and Type II GRBs (ε), supporting a hybrid origin. GRB 230307A (marked in orange) and GRB 211211A (marked in yellow) are overlaid, demonstrating their positions relative to the classical GRB populations. The black and red dashed lines show the $T_{90,i} = 5$ s, and $\varepsilon = 0.03$, respectively.

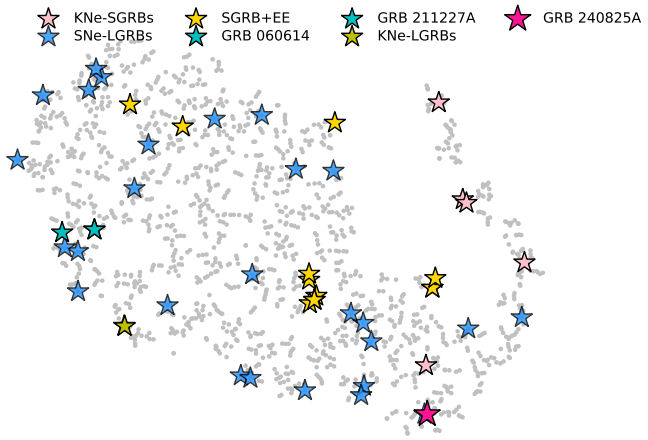


Figure 14. t-SNE classification map of Swift GRBs using normalized, Fourier-transformed prompt light curves as in C. K. Jespersen et al. (2020). GRB 240825A is marked with a pink star and lies near the Type-L (long) GRB cluster. Nonspecial GRBs are shown as small gray points. Light pink stars represent "known mergers," blue stars denote "known collapsars" (e.g., GRB 190829A), and green stars represent the long mergers GRB 060614 and GRB 211227A.

4.4. Search for Associated SNe with GRB 240825A

GRB 240825A exhibits a duration of approximately 4 s and lies at a redshift of $z = 0.659$, placing it relatively nearby in the cosmological context. The burst released a substantial fluence of $\sim 10^{-4}$ erg cm^{-2}, indicative of a highly energetic event and consistent with the Amati relation of collapsar GRBs. Furthermore, its X-ray afterglow luminosity is also consistent with those observed in collapsar GRBs, and significantly more luminous than typical Type I GRBs of merger origin (R. Ruffini et al. 2024). These observational signatures support the classification of GRB 240825A as a likely collapsar event.

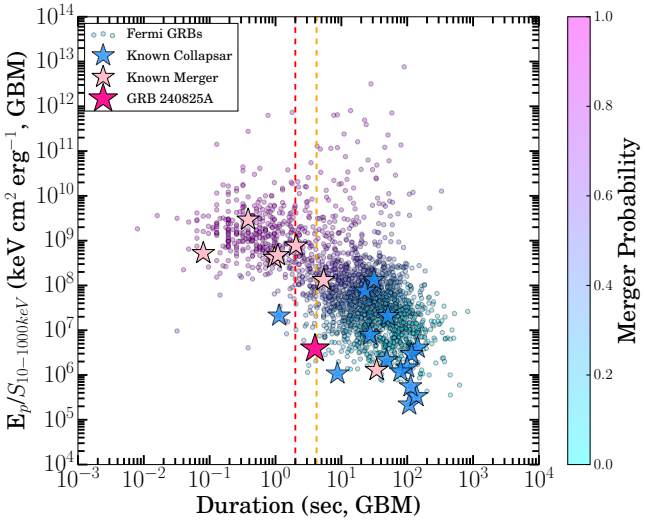


Figure 15. ML classification of GRB 240825A (shown with a pink star) in the plane of burst duration (T_{90}) vs. spectral peak energy over fluence (E_p/S), following the SVM-based method of P. Nuessle et al. (2024). The color scale represents the predicted merger probability, ranging from 1 (merger-like) to 0 (collapsar-like). Known collapsars (blue stars) and known mergers (pink stars) are also shown for reference. GRB 240825A falls in a region with intermediate T_{90} and moderate E_p/S, with a classifier prediction of ∼76% probability for a collapsar origin. The vertical orange and red lines show a 4.2 s duration boundary from the fourth Fermi Catalog (A. von Kienlin et al. 2020) and $T_{90} = 2$ s, respectively.

Its properties are broadly consistent with the binary-driven hypernova (BdHN I) scenario (e.g., C. L. Bianco et al. 2024), indicating a core-collapse progenitor and an associated SN (R. Ruffini et al. 2024). These properties of GRB 240825A motivated us to search for an accompanying SN signature. We conducted a comprehensive search for SN associated with the long-duration burst GRB 240825A, located at a redshift of $z = 0.659$, using optical (using the LBC mounted on the Large Binocular Telescope; E. Giallongo et al. 2008), UV (Swift-UVOT), and NIR (using EMIR mounted on the 10.4 m GTC Telescope) observations. Optical observations were performed in the Sloan r' and z' bands across three epochs: 2024 September 12 (∼17.59 days postburst), 2024 September 28 (∼33.70 days postburst), and 2024 November 9 (∼75.52 days postburst). With a time dilation factor of $1 + z = 1.659$ due to the redshift, these epochs correspond to rest-frame times of approximately 10.60, 20.31, and 45.52 days, respectively, aligning with the typical rise and decay phases of SN-GRB light curves (Z. Cano et al. 2017b). Furthermore, Swift-UVOT performed a deep late-time search for SN emission in the U band up to ∼33.14 days postburst (see Table A3). We also utilized GTC NIR observations in the J, H, and K bands, spanning ∼19.31–27.41 days post-trigger (∼11.6–16.5 rest-frame days), a period optimal for detecting SN emission near its peak (Z. Cano et al. 2017a). The choice of r', z', J, H, and K bands leverages their red and NIR coverage, ideal for detecting redshifted optical emission from a distant source at $z = 0.659$, where rest-frame ultraviolet and blue light are shifted into these wavelengths.

To identify a potential SN signature superimposed on the host galaxy's light, we employed image subtraction using the `AutoPhot` software package (S. J. Brennan & M. Fraser 2022), which implements the `HOTPANTS` algorithm for optimal difference imaging (A. Becker 2015). This technique aligns a science image (containing the potential transient) with a template image (where the transient has faded), scales them to match in flux, and subtracts the template to remove static sources like the host galaxy. For GRB 240825A, the third epoch (2024 November 9, 75.52 days postburst) served as the template, as any SN would have significantly faded by this late time (45.52 rest-frame days), leaving primarily the host galaxy emission. This template was subtracted from the first (2024 September 12) and second (2024 September 28) epoch LBT images in both the r' and z' bands.

The resulting difference images revealed no significant residual flux at the precise position of GRB 240825A, indicating the absence of a detectable SN component (see Figure 16). For the GTC NIR data, the second epoch (∼27.41 days) was subtracted from the first epoch (∼19.31 days) in the J and K bands. No significant residual flux was detected in any difference images at the GRB position (derived from XRT and UVOT uncertainty circles), further indicating the absence of an SN signature. Given the nondetection of a transient source, we calculated upper limits on the brightness of any potential SN. These limits represent the faintest magnitudes detectable at a 3σ confidence level above the background noise in the difference images. For the LBT optical data, the limits are on 2024 September 12, $r' > 25.0$ mag, $z' > 24.8$ mag; on 2024 September 28, $r' > 24.5$ mag, $z' > 23.8$ mag; and on 2024 November 9, $r' > 25.9$ mag, $z' > 25.0$ mag (AB system). For the GTC NIR data, limits at the first epoch (∼19.31–27.41 days) are $J > 23.4$ mag, $H > 23.3$ mag, and $K > 23.1$ mag (AB system). These values reflect the sensitivity of the observations, with variations likely due to differences in seeing conditions, exposure times, or sky brightness across epochs. Furthermore, using the UVOT data, we attempted a deep late-time search for emission from an SN potentially associated with the GRB; however, no evidence of any SN was detected up to 23.4 mag (AB) in the U band. We limit our search to the U band, since it is the most sensitive of UVOT's filters, and this GRB has the most late-time coverage in the U filter. We summed the last three observations and then calculated the upper limits using `uvotsource` (see Table A3). To obtain even deeper limits, we then continued to sequentially add the prior segment's U-band exposure.

To interpret these nondetections, we compared our upper limits to the light curves of well-characterized SN-GRBs: SN 1998bw (associated with GRB 980425, T. J. Galama et al. 1998), SN 2006aj (GRB 060218, S. Campana et al. 2006), SN 2010bh (GRB 100316D, R. L. C. Starling et al. 2011), and SN 2017iuk (GRB 171205A, L. Izzo et al. 2019). These light curves were adjusted to the redshift of GRB 240825A ($z = 0.659$) by applying a time dilation factor of 1.659 and a distance modulus correction to account for luminosity distance differences. The LBT limits do not rule out the full range of known GRB-SNe. In particular, the limits at 33.70 and 75.52 observer-frame days lie above most of the comparison light curves. The earliest epoch at ∼17.59 observer-frame days provides the most useful constraint ($r' > 25.0$ AB mag) and mildly disfavors a very luminous SN 1998bw-like component at that phase (see the light-curve comparison in Figure 17). However, fainter or more slowly evolving events, including SN 2022xiw/GRB 221009A (G. P. Srinivasaragavan et al. 2023) and SN 2026fgk/GRB 260310A (B. O'Connor et al. 2026), would remain consistent with our measurements. The nondetection also suggests either a low-luminosity SN component below our detection limits or a GRB without a

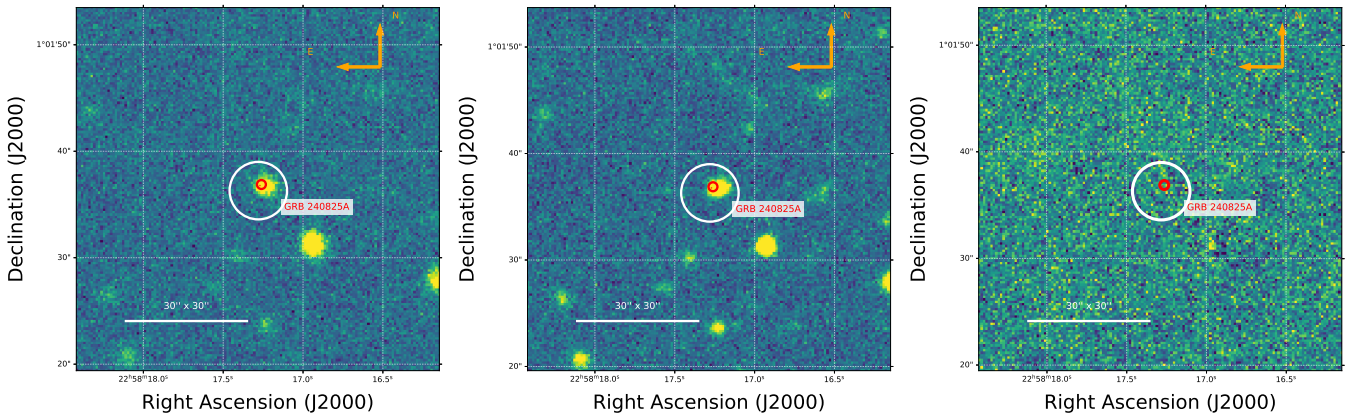


Figure 16. Lack of bright SN associated with GRB 240825A. Left: LBT r'-band image of the GRB 240825A field on 2024 September 28 (∼33.70 days postburst). Middle: LBT r' band on 2024 November 9 (∼ 75.52 days) used as the subtraction template. Right: difference image (September 28–November 9) produced with AutoPhot/HOTPANTS, showing no pointlike residual at the GRB afterglow position (red circle). The white and red circles show the uncertainty in the position measured by Swift-XRT and Swift-UVOT. Images are oriented with north up and east to the left. The scale bar corresponds to 10″.

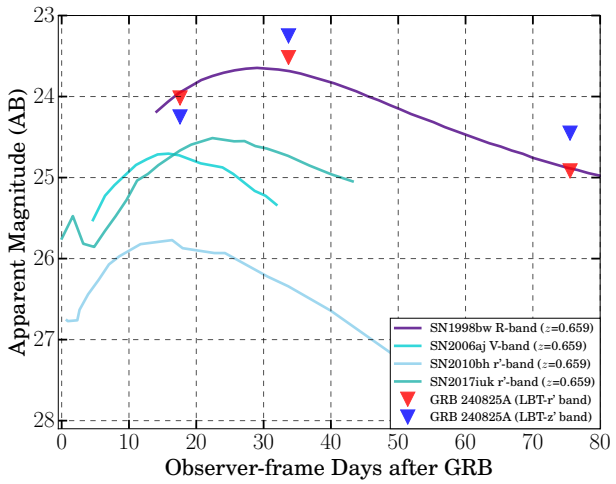


Figure 17. Comparison of our deep optical limits (extinction corrected) for GRB 240825A with well-studied GRB-associated SNe. Optical deep limits in the r and z bands from LBT observations of GRB 240825A, compared to SN 1998bw, SN 2006aj, SN 2010bh, and SN 2017iuk (G. Finneran et al. 2025), scaled to the redshift of GRB 240825A ($z = 0.659$).

detectable SN, potentially indicating diverse physical mechanisms or progenitor properties (A. M. Soderberg et al. 2010). Our NIR limits ($J > 23.4$, $H > 23.3$, and $K > 23.1$ AB mag at ∼19.3–27.4 days after the burst) obtained using GTC provide useful ancillary nondetections at redder wavelengths, where dust extinction is reduced. These limits further strengthen the constraint against a bright SN.

For the nondetection of an SN associated with GRB 240825A, observed using the LBT with an r-band magnitude limit of $m_r > 25.0$ at approximately 17.59 days postburst (observer frame), we derived an extinction-corrected absolute magnitude upper limit of $M_r > -18.68$ mag (with k-correction). Applying a bolometric correction of −0.43 to account for flux outside the observed band (S. J. Prentice et al. 2016), we obtained a bolometric absolute magnitude limit of $M_{\rm bol} > -19.11$ (with k-correction), corresponding to a bolometric luminosity upper limit of $L_{\rm bol} < 1.33 \times 10^{43}\,{\rm erg\,s^{-1}}$. Assuming that any accompanying SN would be powered by the radioactive decay chain ^{56}Ni→^{56}Co→^{56}Fe (e.g., W. D. Arnett 1982; S. Valenti et al. 2008; Y. D. Hu et al. 2021), we used the standard heating function, which relates the bolometric luminosity to the nickel mass via $L_{\rm bol}(t) = \frac{M_{\rm Ni}}{M_\odot} \cdot [(\varepsilon_{\rm Ni} - \varepsilon_{\rm Co})e^{-t/t_{\rm Ni}} + \varepsilon_{\rm Co}e^{-t/t_{\rm Co}}]$ (D. Branch & J. C. Wheeler 2017), where t is the rest-frame time since explosion. Converting the observer-frame time to rest frame using $t_{\rm rest} = t_{\rm obs}/(1+z) = 17.59/1.659 \approx 10.60$ days, and using standard values $\varepsilon_{\rm Ni} = 7.9 \times 10^{43}\,{\rm erg\,s^{-1}}$, $\varepsilon_{\rm Co} = 1.45 \times 10^{43}\,{\rm erg\,s^{-1}}$, $t_{\rm Ni} = 8.8$ days, and $t_{\rm Co} = 111.3$ days (Z. Bora et al. 2022), we estimate an upper limit on the synthesized nickel mass of $M_{\rm Ni} \lesssim 0.41\,M_\odot$. This limit is consistent with SN 1998bw, which had an $M_{\rm Ni} \approx 0.4\,M_\odot$ (K. Iwamoto et al. 1998), while SN 2003dh had a lower value of $M_{\rm Ni} \approx 0.35\,M_\odot$ (P. A. Mazzali et al. 2003). As the amount of nickel synthesized determines the peak of an SN powered by the radioactive decay chain ^{56}Ni→^{56}Co→^{56}Fe, the inferred $M_{\rm Ni}$ suggests that any accompanying SN to GRB 240825A must be faint.

To search for a potential SN associated with GRB 240825A, we obtained late-time photometry in the observer-frame z band, which probes the rest-frame V band at the burst redshift ($z = 0.659$). Based on our nondetections, we derive upper limits on the absolute magnitude. For rest-frame SN peak times of 10.60 days (17.59 observer-frame days) and 20.31 days (33.70 observer-frame days), the limits correspond to $M_V > -18.73$ and $M_V > -19.73$, respectively. The 17.59 day limit is the deepest optical constraint and could be relevant if the associated SN were fast-evolving and peaked at an early rest-frame time of ∼10 days, as seen in some rapidly evolving GRB-SNe. In this case, the nondetection would imply that such a fast SN was fainter than $M_V \simeq -18.73$. However, this epoch is earlier than the expected observer-frame peak of an SN 1998bw-like template at $z = 0.659$. For a broader, SN 1998bw-like light curve, the 33.70 day limit is the more appropriate comparison, and this constraint is substantially milder. We placed these values of GRB 240825A in the distribution of peak absolute V-band magnitude (M_V) versus rest-frame peak time ($T_{\rm max}$) for GRB-associated SNe. This constraint is shown in Figure 18 (we emphasize that, because no SN component was detected, the peak time of any associated SN is not directly measured. Therefore, the limits should be interpreted as epoch-dependent upper limits), alongside the GRB-SN sample from S. O. Belkin & A. S. Pozanenko (2024). Our observations show that no bright SN component was detected at either an early-/fast-SN epoch or near the expected peak epoch of a broader GRB-SN.

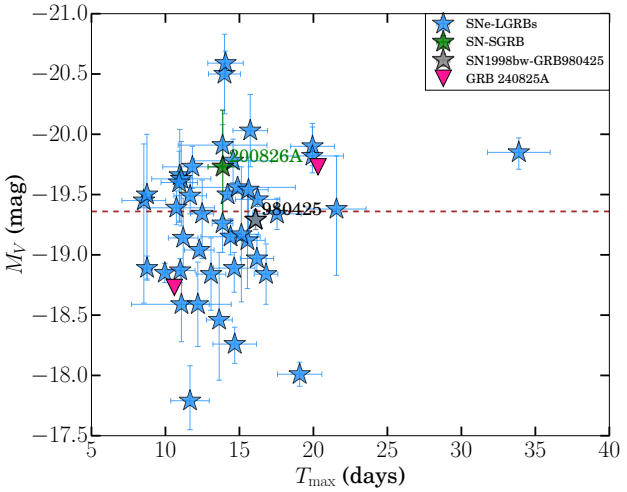


Figure 18. Distribution of peak absolute V-band magnitude (M_V) vs. rest-frame peak time ($T_{\rm max}$) for GRB-associated SN. Blue stars represent SNe-long-duration GRBs, green stars denote SN-SGRB (GRB 200826A), and the gray star marks SN 1998bw associated with GRB 980425. The pink triangles indicate the GRB 240825A upper limits (derived from our z-band observations) at the actual observing epochs: 17.59 and 33.70 days in the observer frame, corresponding to 10.60 and 20.31 days in the rest frame, respectively. The earlier 17.59 day limit may be interpreted as a constraint on a fast/early-peaking GRB-SN, whereas the 33.70 day limit is more relevant for a broader, SN 1998bw-like event whose observed peak would be expected closer to ∼30 days after the burst. Data points for comparison are taken from S. O. Belkin & A. S. Pozanenko (2024), and the brown dashed line marks the median peak brightness of the SN-long-duration GRB population.

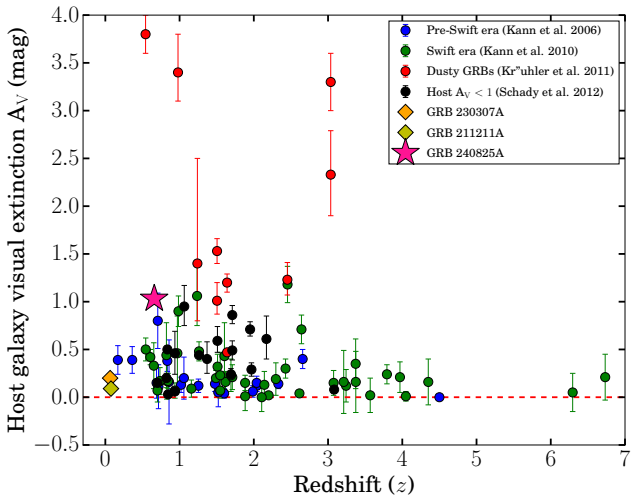


Figure 19. The figure illustrates the relationship between host galaxy visual extinction (A_V) and redshift (z) for GRB 240825A alongside various GRB samples, with the horizontal red dashed line indicating $A_V = 0$. Our analysis reveals that GRB 240825A exhibits a significantly elevated A_V at its redshift relative to the broader GRB population.

The nondetection therefore argues against a luminous, unobscured SN peaking near the observed epochs, but it does not exclude a normal, moderately faint, or dust-obscured GRB-SN.

We explored the possible cause (such as the local environment) of the nondetection of the associated SN for GRB 240825A. The visual extinction (A_V), defined as the attenuation of light in the visual band due to dust along the line of sight, serves as a critical indicator of the dust content and density of the ISM. Based on the afterglow analysis using UVOT and XRT data, we derive a color excess of ($E(B-V) = 0.35 \pm 0.03$ mag) and a visual extinction of ($A_V \sim 1.03$ mag) for LMC, indicating significant dust attenuation along the line of sight of GRB 240825A. In this study, we investigate the A_V as a function of redshift (z) for GRB 240825A, comparing it with a well-established sample of GRBs from prior works (D. A. Kann et al. 2006, 2010; T. Krühler et al. 2011; P. Schady et al. 2012). This high LOS extinction places GRB 240825A among the more dust-obscured events at its redshift relative to the broader GRB population, suggesting an unusually dust-rich host galaxy (see Figure 19). Notably, despite extensive follow-up observations in the NIR, UV, and optical bands, no SN counterpart was detected for GRB 240825A, which could be attributed to this substantial dust obscuration. An intrinsically faint SN also remains consistent with the observational limits. Across the GRB sample, we observe a general trend of decreasing A_V with increasing redshift, likely driven by selection biases inherent in high-redshift observations (D. A. Kann et al. 2010; R. Gupta et al. 2022b; A. J. Castro-Tirado et al. 2024).

5. Conclusion

In this study, we have performed a detailed, multiwavelength investigation of GRB 240825A-a unique gamma-ray burst that challenges the traditional dichotomy between short and long GRBs. Classical diagnostics such as its high fluence, energetics, positive spectral lag, placement within the $E_{\rm p,i}$–$E_{\gamma,\rm iso}$ (Amati) relation, and a massive, dusty, star-forming host favor an interpretation more consistent with collapsar-driven long GRBs. To further refine its classification, we employed advanced ML classifiers (e.g., t-SNE, SVMs) and modern physical metrics such as the EHD parameter and $\varepsilon = E_{\gamma,\rm iso,52}/E^{5/3}_{p,z,2}$. The SVM classifier assigns a 76% probability of collapsar origin, and the EH/EHD and ϵ parameters place GRB 240825A firmly in the Type II (collapsar) region.

Late-time photometric and spectroscopic follow-up with the 10.4 m GTC, LBT, and Swift-UVOT revealed no detectable SN component down to deep limits ($m_r > 25.0$, $m_J > 23.4$, $m_H > 23.3$, and $m_K > 23.1$ AB mag), despite a relatively nearby redshift of $z = 0.659$. The deepest 17.59 day LBT limit constrains a possible fast/early-peaking SN, while the 33.70 day limit is more relevant for a broader SN 1998bw-like event. Taken together, the observations rule out only a sufficiently bright SN peaking near the observed epochs. The absence of bright SN features, especially those similar to SN 1998bw, raises two possibilities: either the SN was intrinsically faint (low-luminosity SN with absolute magnitude M_V fainter than -18.5 mag), or it was heavily extinguished by dust in the host environment. We therefore interpret GRB 240825A as a collapsar-favored GRB with no detected luminous SN along a dusty sightline.

In summary, GRB 240825A is an archetypal example of a GRB that lies near the boundary of current classification schemes. This burst reinforces the need for a unified framework that combines prompt emission physics, afterglow behavior, host galaxy properties, and contextual progenitor signatures. Future studies, particularly those leveraging high-cadence multiwavelength follow-up and statistical learning techniques, will be essential to identify and interpret such events within the broader landscape of GRB phenomenology. Additionally, JWST mid-infrared follow-up could potentially detect dust-reprocessed SN emission and definitively resolve the nature of such events.

Acknowledgments

We sincerely thank the referee for their thorough and valuable suggestions, which have significantly improved the quality of our manuscript. R.G. was sponsored by the National Aeronautics and Space Administration (NASA) through a contract with ORAU. The views and conclusions contained in this document are those of the authors and should not be interpreted as representing the official policies, either expressed or implied, of the National Aeronautics and Space Administration (NASA) or the US Government. The US Government is authorized to reproduce and distribute reprints for government purposes notwithstanding any copyright notation herein. A.R. acknowledges support by PRIN-MIUR 2017 (grant 20179ZF5KS). A.J.C.T. acknowledges support from the Spanish Ministry project PID2023-151905OB-I00 and Junta de Andalucía grant P20_010168 and from the Severo Ochoa grant CEX2021-001131-S funded by MCIN/AEI/10.13039/501100011033. Based on observations collected at the Observatorio de Sierra Nevada (operated by IAA-CSIC) and at the Centro Astronómico Hispano en Andalucía (CAHA) at Calar Alto (proposal 24B-2.2-010), operated jointly by Junta de Andalucía and Consejo Superior de Investigaciones Científicas (IAA-CSIC). Also based on observations made with the Gran Telescopio Canarias (GTC) (proposal GTCMULTIPLE7B-24B 104-MULTIPLE-7/24A), installed at the Spanish Observatorio del Roque de los Muchachos of the Instituto de Astrofísica de Canarias, on the island of La Palma. This work is partly based on data obtained with the instrument OSIRIS, built by a Consortium led by the Instituto de Astrofísica de Canarias in collaboration with the Instituto de Astronomía of the Universidad Autónoma de México. OSIRIS was funded by GRANTECAN and the National Plan of Astronomy and Astrophysics of the Spanish Government. M.C.G. acknowledges support from the Spanish Ministry project PID2023-149817OB-C31. The program of development within Priority-2030 is acknowledged for supporting the research at UrFU. ASIM is a mission of ESA's SciSpace program for scientific utilization of the ISS and non-ISS space exploration platforms and space environment analogues. ASIM and the ASIM Science Data Centre are funded by ESA and by national grants of Denmark, Norway and Spain. This research has used data obtained through the HEASARC Online Service, provided by the NASA-GSFC, in support of NASA High Energy Astrophysics Programs. This work made use of data supplied by the UK Swift Science Data Centre at the University of Leicester. The LBT is an international collaboration of the University of Arizona, Italy (INAF: Istituto Nazionale di Astrofisica), Germany (LBTB: LBT Beteiligungsgesellschaft), The Ohio State University, representing also the University of Minnesota, the University of Virginia, and the University of Notre Dame. L.H. acknowledges support from Research Ireland grant 19/FFP/6777. D.T. acknowledges support from the National Research Foundation of Korea (NRF) grant, RS-2024-00343729, funded by the Korean government (MSIT).

Facilities: Swift (BAT, XRT and UVOT), Fermi, , GTC, LBT, OSN.

Software: `astropy` (Astropy Collaboration et al. 2013, 2018; Astropy Collaboration et al. 2022), `XSPEC` (K. A. Arnaud 1996), Source Extractor (E. Bertin & S. Arnouts 1996).

Appendix
Figures and Tables

This appendix presents the supplementary Figures (A1 and A2) and Tables (A1, A2, and A3) corresponding to the analyses described in the main text.

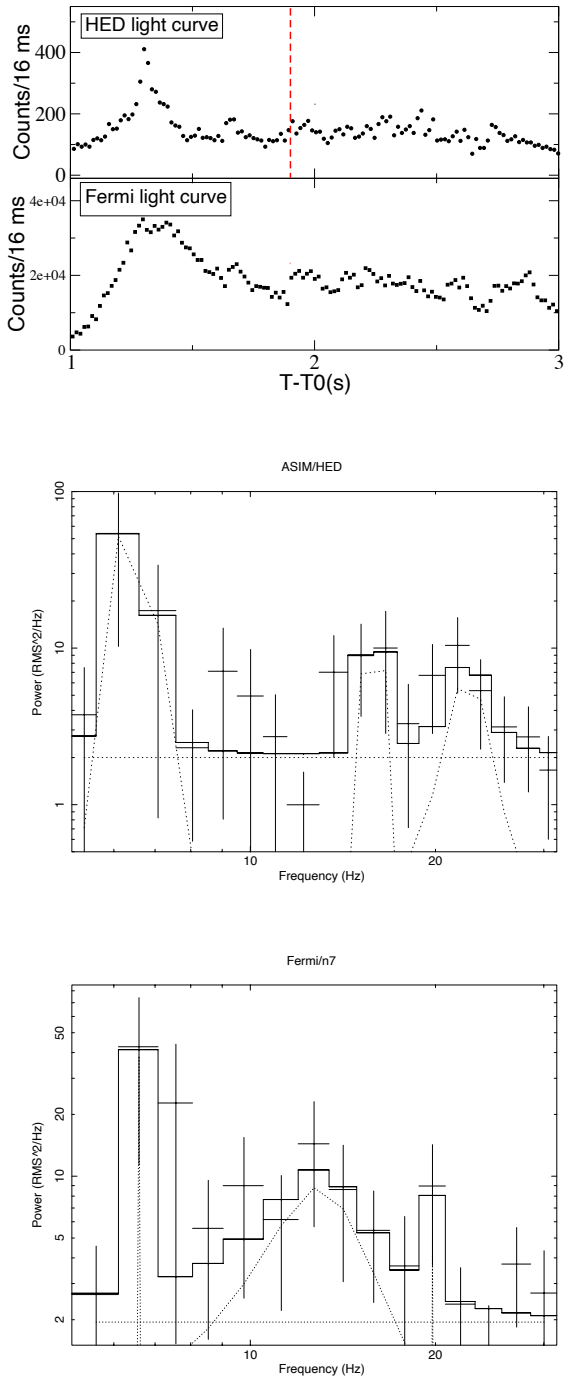


Figure A1. Top: barycentred ASIM (HED; 0.3–20 MeV) and Fermi (GBM; 150–30 MeV) light curves of GRB 240825A showing the time intervals ($T_0 + 1.9$ to $T_0 + 3.0$ s and $T_0 + 1.0$ to $T_0 + 3.0$ s) where the timing analysis was performed. Middle and bottom: the PDS of the ASIM-HED (0.3–20 MeV) and Fermi/NaI-7 (8–800 keV) light curves of GRB 240825A at the time intervals of 1.9−3.0 s and 1.0–3.0 s, where T_0 is the Fermi trigger time.

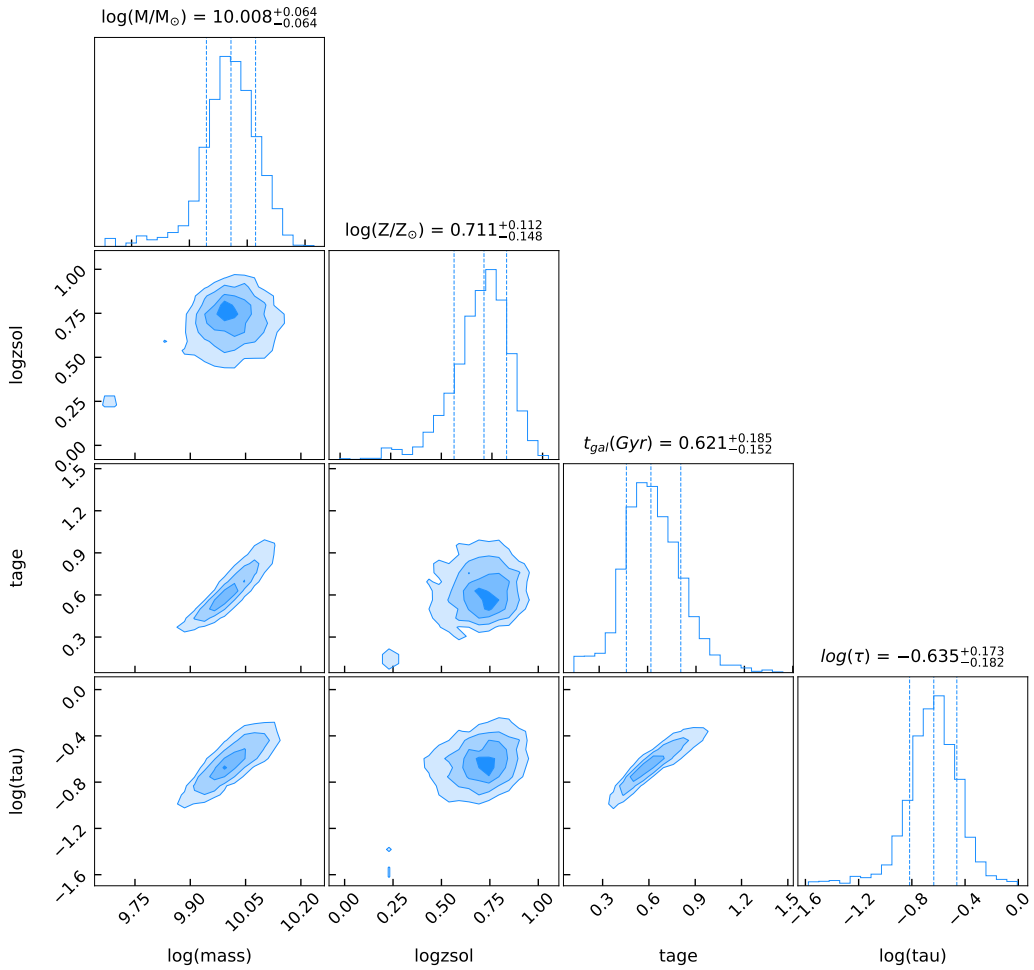


Figure A2. Corner plot illustrating the posterior distributions of host SED model parameters obtained using `Prospector`: stellar mass ($\log(M/M_{\odot})$) and star formation timescale ($\log(\tau\ \mathrm{yr}^{-1})$), dust, from the MCMC fitting process. The contours represent 68% and 95% confidence intervals. The best-fit values are marked with blue lines.

Table A1
Optical/UV Follow-up Observations of GRB 240825A

Telescope	Filter	$T - T_0$ (s)	Exp. (s)	Mag.	Mag. Err.	System
Swift-UVOT	WH	102.99740	10.00000	15.612	0.036	AB
Swift-UVOT	WH	122.99740	10.00000	15.871	0.037	AB
Swift-UVOT	WH	142.99740	10.00000	16.253	0.041	AB
Swift-UVOT	WH	167.99740	15.00000	16.470	0.035	AB
Swift-UVOT	WH	202.99740	20.00000	16.781	0.034	AB
Swift-UVOT	WH	232.87380	9.87640	16.976	0.052	AB
Swift-UVOT	WH	594.91400	9.88150	18.365	0.104	AB
Swift-UVOT	WH	767.51850	9.87600	18.574	0.118	AB
Swift-UVOT	WH	1170.87090	9.87590	19.161	0.206	AB
Swift-UVOT	WH	6095.52310	99.89210	20.586	0.165	AB
Swift-UVOT	*V*	77.82920	5.00000	13.625	0.068	AB
Swift-UVOT	*V*	644.85540	9.87690	16.997	0.261	AB
Swift-UVOT	*V*	817.11690	9.88140	17.025	0.266	AB
Swift-UVOT	*V*	1134.47400	96.11000	17.661	0.298	AB
Swift-UVOT	*V*	5069.72090	99.88650	19.098	0.424	AB
Swift-UVOT	*V*	10,883.36850	453.36470	20.196	0.538	AB
Swift-UVOT	*V*	53,432.26540	3390.49850	>20.059	⋯	AB
Swift-UVOT	*V*	81,813.87990	3405.69650	>20.121	⋯	AB
Swift-UVOT	*B*	570.52030	9.88160	17.393	0.185	AB
Swift-UVOT	*B*	743.22400	9.87600	17.650	0.220	AB
Swift-UVOT	*B*	1146.45580	9.87660	18.845	0.795	AB
Swift-UVOT	*B*	5890.87900	99.88650	20.240	0.616	AB
Swift-UVOT	*U*	335.41420	30.00000	17.767	0.087	AB
Swift-UVOT	*U*	405.41420	40.00000	18.035	0.087	AB
Swift-UVOT	*U*	490.41420	45.00000	18.057	0.083	AB
Swift-UVOT	*U*	545.29720	9.88300	18.240	0.210	AB
Swift-UVOT	*U*	718.32840	9.88170	18.990	0.357	AB
Swift-UVOT	*U*	1204.12500	92.42510	19.120	0.382	AB
Swift-UVOT	*U*	5685.01030	99.89210	20.318	0.279	AB
Swift-UVOT	*U*	40,602.84590	329.04030	>21.426	⋯	AB
Swift-UVOT	*U*	143,988.61540	8738.43570	>22.226	⋯	AB
Swift-UVOT	*U*	178,393.99880	9192.96970	>22.249	⋯	AB
Swift-UVOT	*U*	246,282.46700	20,264.49860	>22.406	⋯	AB
Swift-UVOT	*U*	377,364.80130	37,202.24030	>23.069	⋯	AB
Swift-UVOT	*U*	425,514.30050	692.72390	22.834	1.586	AB
Swift-UVOT	UVW1	5480.11240	99.88650	20.929	0.383	AB
Swift-UVOT	UVW1	347,58.21760	408.60420	>22.214	⋯	AB
Swift-UVOT	UVM2	5274.65740	99.88650	21.945	0.884	AB
Swift-UVOT	UVM2	11,449.02620	107.17380	22.714	3.395	AB
Swift-UVOT	UVW2	4865.04370	99.88100	>21.426	⋯	AB
Swift-UVOT	UVW2	6301.23740	99.88650	22.303	1.101	AB
Swift-UVOT	UVW2	44,520.64640	266.27400	23.028	1.960	AB
Swift-UVOT	UVW2	86,962.40790	2930.34870	>23.389	⋯	AB
OSN	*B*	30,176	300	21.43	0.17	AB
OSN	*B*	31,419	300	21.46	0.17	AB
OSN	*B*	32,663	300	21.70	0.19	AB
OSN	*B*	33,904	300	21.68	0.22	AB
OSN	*B*	35,769	600	21.72	0.14	AB
OSN	*B*	38,871	900	22.20	0.24	AB
OSN	*V*	30,486	300	20.54	0.15	AB
OSN	*V*	31,762	300	20.41	0.12	AB
OSN	*V*	32,970	300	20.44	0.12	AB
OSN	*V*	34,210	300	20.87	0.18	AB
OSN	*V*	35,455	300	21.25	0.24	AB
OSN	*V*	37,944	900	21.32	0.09	AB
OSN	*I*	31,103	300	19.83	0.07	AB
OSN	*I*	32,348	300	19.93	0.08	AB
OSN	*I*	33,589	300	19.98	0.08	AB
OSN	*I*	34,830	300	19.94	0.08	AB
OSN	*I*	36,077	300	19.99	0.07	AB
OSN	*I*	37,320	300	19.98	0.07	AB
OSN	*I*	38,560	300	19.94	0.08	AB
OSN	*I*	39,801	300	20.00	0.08	AB

Table A1
(Continued)

Telescope	Filter	$T - T_0$ (s)	Exp. (s)	Mag.	Mag. Err.	System
OSN	*I*	41,041	300	20.06	0.09	AB
OSN	*R*	30,796	300	20.22	0.11	AB
OSN	*R*	32,037	300	20.48	0.10	AB
OSN	*R*	33,282	300	20.33	0.10	AB
OSN	*R*	34,521	300	20.38	0.09	AB
OSN	*R*	35,767	300	20.46	0.10	AB
OSN	*R*	37,013	300	20.37	0.09	AB
OSN	*R*	38250	300	20.47	0.12	AB
OSN	*R*	39,493	300	20.52	0.12	AB
OSN	*R*	40,730	300	20.47	0.10	AB
BOOTES-6	*R*	9063	600	19.30	0.18	AB
BOOTES-6	*R*	10,871	1200	19.44	0.18	AB
BOOTES-6	*R*	13,159	1200	19.32	0.10	AB
BOOTES-6	*R*	15,386	1200	19.60	0.10	AB
BOOTES-6	*R*	17,379	1200	20.07	0.11	AB
BOOTES-6	*R*	19,853	1680	20.08	0.11	AB
AZT-22	*R*	7827	300	18.96	0.03	Vega
AZT-22	*R*	8151	300	19.04	0.03	Vega
AZT-22	*R*	8476	300	19.07	0.03	Vega
AZT-22	*R*	8800	300	19.09	0.03	Vega
AZT-22	*R*	9125	300	19.08	0.03	Vega
AZT-22	*R*	9449	300	19.16	0.03	Vega
AZT-22	*R*	108,002	3000	21.46	0.08	Vega
AZT-22	*B*	102,975	4200	22.59	0.09	Vega
AZT-22	*R*	185,045	4200	21.85	0.07	Vega
AZT-22	*R*	268,488	5100	21.85	0.07	Vega
RC-35 (Kitab)	Clear	17,876	3600	>18.30	⋯	Vega
Zeiss-1000 (TSHAO)	*R*	84,755	3600	> 21.30	⋯	Vega
Zeiss-1000 (SAO)	*R*	21,078	3000	> 19.50	⋯	Vega
Zeiss-1000 (SAO)	*R*	115,706	3600	> 21.00	⋯	Vega
Zeiss-1000 (SAO)	*R*	189,626	4200	21.88	0.07	Vega
Zeiss-1000 (SAO)	*R*	274,672	5400	22.15	0.07	Vega

Note. All magnitudes are reported without correction for Galactic or host-galaxy extinction. Swift-UVOT limiting magnitudes correspond to 3σ limits. Swift-UVOT, OSN, and BOOTES-6 mag are reported in the AB system. BOOTES-6 *R*-band magnitudes were converted from Vega to AB magnitudes using a zero-point offset of 0.21 mag. GRB IKI-FuN magnitudes are reported in the Vega system.

Table A2
PDS Timing Analysis Results of the Light Curve from GRB 240825A Using the `lorentzian+lorentzian+lorentzian+powerlaw` Function for Fermi (Upper) and ASIM (Lower) Data

T_{start} (s)	T_{stop} (s)	ν_{QPO1} (Hz)	$FWHM_{QPO1}$ (Hz)	N_{QPO1}	ν_{QPO2} (Hz)	$FWHM_{QPO2}$ (Hz)	N_{QPO2}	Γ_P (Hz)	N_P (Hz)	χ^2 (d.o.f.)
1.0	3.0	$6.2^{+0.7}_{-0.06}$	$(1 \pm 0.1)E - 3$	37 ± 30	$19.5^{+1.6}_{-1.0}$	$(1 \pm 0.1)E - 3$	10 ± 8	0 (f)	1.95 ± 0.8	3.5 (5)
1.9	3.0	$6.5^{+0.10}_{-0.7}$	$0.08^{+0.4}_{-0.07}$	61 ± 50	21.7 ± 1.0	$2.1^{+2.1}_{-1.1}$	33 ± 20	0 (f)	1.75 ± 0.8	5.5 (8)

Note. T_{start} and T_{stop} are referred to with respect to the Fermi reference time ($T_{0,Fermi}$). The errors given are 1σ. ν_{QPO1}, ν_{QPO2} are the frequencies of the QPO features, while $FWHM_{QPO1}$, $FWHM_{QPO2}$, and N_{QPO1}, N_{QPO2} are their full width at half-maximum and normalization for both QPOs, respectively. Γ_P and N_P represent the high-frequency power-law index and normalization, respectively. χ^2 (d.o.f.): chi-squared statistic value with d.o.f. in parentheses, indicating the goodness of fit of the model to the data.

Table A3
Late-time Swift-UVOT Observations for SN Search Associated with GRB 240825A

Start Time (days, $T - T_0$)	Stop Time (days, $T - T_0$)	Exposure (s)	Filter	Mag Limit (AB, 3σ)
24.73	33.14	6030	*U*	22.75
3.94	33.14	7532	*U*	22.87
4.73	33.14	11,070	*U*	23.09
2.62	33.14	14,487	*U*	23.24
1.57	33.14	18,232	*U*	23.37
0.47	33.14	18,872	*U*	23.39

Note. All observations were performed in the UVOT *U* band. Magnitudes represent 3σ upper limits and have not been corrected for Galactic extinction.

ORCID iDs

Rahul Gupta https://orcid.org/0000-0003-4905-7801
Judith Racusin https://orcid.org/0000-0002-4744-9898
R. Sánchez-Ramírez https://orcid.org/0000-0002-7158-5099
Y.-D. Hu https://orcid.org/0000-0002-7400-4608
A. Rossi https://orcid.org/0000-0002-8860-6538
M. D. Caballero-García https://orcid.org/0000-0001-7920-4564
Pi Nuessle https://orcid.org/0000-0001-5939-644X
A. J. Castro-Tirado https://orcid.org/0000-0003-2999-3563
S. R. Oates https://orcid.org/0000-0001-9309-7873
P. P. Bordoloi https://orcid.org/0009-0005-6858-6356
A. Aryan https://orcid.org/0000-0002-9928-0369
S. Dichiara https://orcid.org/0000-0001-6849-1270
P. Veres https://orcid.org/0000-0002-2149-9846
N. Klingler https://orcid.org/0000-0002-7465-0941
N. Omodei https://orcid.org/0000-0002-5448-7577
E. Maiorano https://orcid.org/0000-0003-2593-4355
D. Tak https://orcid.org/0000-0002-9852-2469
S. Shilling https://orcid.org/0009-0009-4622-7749
J. E. Adsuara https://orcid.org/0000-0002-3842-965X
E. Fernández-García https://orcid.org/0009-0009-4604-9639
A. Ghosh https://orcid.org/0000-0003-2265-0381
E. Göğüş https://orcid.org/0000-0002-5274-6790
F. J. Gordillo-Vázquez https://orcid.org/0000-0002-0719-8203
M. Gritsevich https://orcid.org/0000-0003-4268-6277
S. Guziy https://orcid.org/0000-0003-2628-6468
L. Hanlon https://orcid.org/0000-0003-2931-3732
H. J. van Heerden https://orcid.org/0009-0004-9747-7215
S. Iyyani https://orcid.org/0000-0003-3220-7543
A. Martin-Carrillo https://orcid.org/0000-0001-5108-0627
P. J. Meintjes https://orcid.org/0000-0001-8890-5418
J. Navarro-González https://orcid.org/0000-0002-3799-1237
T. Neubert https://orcid.org/0000-0001-7851-7788
N. Østgaard https://orcid.org/0000-0002-2572-7033
I. Pérez-García https://orcid.org/0000-0002-7273-3671
S. Razzaque https://orcid.org/0000-0002-0130-2460
E. Sonbas https://orcid.org/0000-0002-6909-192X
Si-Yu Wu https://orcid.org/0009-0004-7113-8258
A. Pozanenko https://orcid.org/0000-0001-9435-1327
A. Volnova https://orcid.org/0000-0003-3554-1037
A. Moskvitin https://orcid.org/0000-0003-3244-6616
S. Belkin https://orcid.org/0000-0002-9798-029X
Sh. Egamberdiyev https://orcid.org/0000-0001-9730-3769
V. Rumyantsev https://orcid.org/0000-0003-1894-7019
Jan Snigula https://orcid.org/0000-0003-4044-5357
Chiara Ventura https://orcid.org/0009-0009-9751-9215

References

Ahumada, T., Singer, L. P., Anand, S., et al. 2021, NatAs, 5, 917
Amati, L., Frontera, F., Tavani, M., et al. 2002, A&A, 390, 81
Arnaud, K. A. 1996, ASPC, 101, 17
Arnett, W. D. 1982, ApJ, 253, 785
Astropy Collaboration, Price-Whelan, A. M., Lim, P. L., et al. 2022, ApJ, 935, 167
Astropy Collaboration, Price-Whelan, A. M., Sipőcz, B. M., et al. 2018, AJ, 156, 123
Astropy Collaboration, Robitaille, T. P., Tollerud, E. J., et al. 2013, A&A, 558, A33
Becker, A. 2015, HOTPANTS: High Order Transform of PSF ANd Template Subtraction, Astrophysics Source Code Library, ascl:1504.004
Belkin, S. O., & Pozanenko, A. S. 2024, AstL, 50, 701
Berger, E. 2014, ARA&A, 52, 43
Bernardini, M. G., Ghirlanda, G., Campana, S., et al. 2015, MNRAS, 446, 1129
Bertin, E., & Arnouts, S. 1996, A&AS, 117, 393
Bianco, C. L., Mirtorabi, M. T., Moradi, R., et al. 2024, ApJ, 966, 219
Blanchard, P. K., Berger, E., & Fong, W.-f. 2016, ApJ, 817, 144
Bloom, J. S., Kulkarni, S. R., & Djorgovski, S. G. 2002, AJ, 123, 1111
Bora, Z., Vinkó, J., & Könyves-Tóth, R. 2022, PASP, 134, 054201
Branch, D., & Wheeler, J. C. 2017, Supernova Explosions (Springer)
Breeveld, A. A., Landsman, W., Holland, S. T., et al. 2011, PASP, 134, 054201
Brennan, S. J., & Fraser, M. 2022, A&A, 667, A62
Brivio, R., Ferro, M., D'Avanzo, P., et al. 2024, GCN, 37295, 1
Bromberg, O., Nakar, E., Piran, T., & Sari, R. 2013, ApJ, 764, 179
Burrows, D. N., Hill, J. E., Nousek, J. A., et al. 2005, SSRv, 120, 165
Caballero-García, M. D., Göğüş, E., Navarro-González, J., et al. 2025, MNRAS, 538, L100
Caballero-García, M. D., Gupta, R., Pandey, S. B., et al. 2023, MNRAS, 519, 3201
Camisasca, A. E., Guidorzi, C., Amati, L., et al. 2023, A&A, 671, A112
Campana, S., Mangano, V., Blustin, A. J., et al. 2006, Natur, 442, 1008
Cano, Z., Izzo, L., de Ugarte Postigo, A., et al. 2017a, A&A, 605, A107
Cano, Z., Wang, S.-Q., Dai, Z.-G., & Wu, X.-F. 2017b, AdAst, 2017, 8929054
Castro-Tirado, A. J. 2023, NatAs, 7, 1136
Castro-Tirado, A. J., Gupta, R., Pandey, S. B., et al. 2024, A&A, 683, A55
Cheng, Y., Pan, Y., Yang, Y.-P., et al. 2025, ApJ, 979, 38
Dainotti, M. G., Lenart, A. Ł., Sarracino, G., et al. 2020, ApJ, 904, 97
Della Valle, M., Chincarini, G., Panagia, N., et al. 2006, Natur, 444, 1050
Di Lalla, N., Gupta, R., Holzmann, A. & Fermi-LAT Collaboration 2024, GCN, 37288, 1
Evans, P. A., Beardmore, A. P., Page, K. L., et al. 2007, A&A, 469, 379
Evans, P. A., Beardmore, A. P., Page, K. L., et al. 2009, MNRAS, 397, 1177
Evans, P. A., Goad, M. R., Osborne, J. P., Beardmore, A. P. & Swift-XRT Team 2024, GCN, 37290, 1
Fermi GBM Team 2024, GCN, 37273, 1
Finneran, G., Cotter, L., & Martin-Carrillo, A. 2025, A&C, 52, 100954
Fong, W., Berger, E., Chornock, R., et al. 2013, ApJ, 769, 56
Fong, W., Berger, E., & Fox, D. B. 2010, ApJ, 708, 9
Fong, W.-f., Nugent, A. E., Dong, Y., et al. 2022, ApJ, 940, 56
Fontana, A., Dunlop, J. S., Paris, D., et al. 2014, A&A, 570, A11
Frederiks, D., Lysenko, A., Ridnaia, A., et al. 2024, GCN, 37302, 1
Fruchter, A. S., Levan, A. J., Strolger, L., et al. 2006, Natur, 441, 463
Fynbo, J. P. U., Watson, D., Thöne, C. C., et al. 2006, Natur, 444, 1047
Galama, T. J., Vreeswijk, P. M., van Paradijs, J., et al. 1998, Natur, 395, 670
Gao, H., Lei, W.-H., Zou, Y.-C., Wu, X.-F., & Zhang, B. 2013, NewAR, 57, 141
Gehrels, N., Norris, J. P., Barthelmy, S. D., et al. 2006, Natur, 444, 1044
Giallongo, E., Ragazzoni, R., Grazian, A., et al. 2008, A&A, 482, 349
Golkhou, V. Z., Butler, N. R., & Littlejohns, O. M. 2015, ApJ, 811, 93
Granot, J., & Sari, R. 2002, ApJ, 568, 820
Gulati, A., Leung, J. K., & Anderson, G. E. 2024, GCN, 37388, 1
Gupta, R. 2023, arXiv:2312.16265
Gupta, R., Brivio, R., Dichiara, S., et al. 2024a, GCN, 37274, 1
Gupta, R., Gupta, S., Chattopadhyay, T., et al. 2022a, MNRAS, 511, 1694
Gupta, R., Oates, S. R., Pandey, S. B., et al. 2021, MNRAS, 505, 4086

Gupta, R., Pandey, S. B., Gupta, S., et al. 2024b, ApJ, 972, 166
Gupta, R., Pandey, S. B., Kumar, A., et al. 2022b, JApA, 43, 82
Gupta, R., Racusin, J., Oganesyan, G., et al. 2026, arXiv:2606.28267
Gupta, R., Ror, A. K., Pandey, S. B., et al. 2025, in VII Workshop on Robotic Autonomous Observatories, 59, (Revista Mexicana de Astrofísica y Astronomía Serie de Conferencias), 115
Hjorth, J., Sollerman, J., Møller, P., et al. 2003, Natur, 423, 847
Hu, Y. D., Castro-Tirado, A. J., Kumar, A., et al. 2021, A&A, 646, A50
Hu, Y. D., Fernández-García, E., Caballero-García, M. D., et al. 2023, FrASS, 10, 952887
Iwamoto, K., Mazzali, P. A., Nomoto, K., et al. 1998, Natur, 395, 672
Izzo, L., & Malesani, D. B. 2024, GCN, 37287, 1
Izzo, L., de Ugarte Postigo, A., Maeda, K., et al. 2019, Natur, 565, 324
Jespersen, C. K., Severin, J. B., Steinhardt, C. L., et al. 2020, ApJL, 896, L20
Joshi, J., Waratkar, G., Vibhute, A., et al. 2024, GCN, 37298, 1
Kalberla, P. M. W., Burton, W. B., Hartmann, D., et al. 2005, A&A, 440, 775
Kann, D. A., Klose, S., & Zeh, A. 2006, ApJ, 641, 993
Kann, D. A., Klose, S., Zhang, B., et al. 2010, ApJ, 720, 1513
Kouveliotou, C., Meegan, C. A., Fishman, G. J., et al. 1993, ApJL, 413, L101
Krühler, T., Greiner, J., Schady, P., et al. 2011, A&A, 534, A108
Kuin, N. P. M., Gupta, R. & Swift/UVOT Team 2024, GCN, 37296, 1
Kumar, P., & Panaitescu, A. 2000, ApJL, 541, L51
Laskar, T., Alexander, K. D., Christy, C., et al. 2024, GCN, 37314, 1
Le Floc'h, E., Adami, C., Schneider, B., et al. 2024, GCN, 37300, 1
Lenart, A., Dainotti, M. G., Khatiya, N., et al. 2025, JHEAp, 47, 100384
Lien, A., Sakamoto, T., Barthelmy, S. D., et al. 2016, ApJ, 829, 7
Levan, A. J., Gompertz, B. P., Salafia, O. S., et al. 2024, Natur, 626, 737
Lü, H.-J., Liang, E.-W., Zhang, B.-B., & Zhang, B. 2010, ApJ, 725, 1965
Lü, H.-J., Yuan, H.-Y., Yi, T.-F., et al. 2022, ApJL, 931, L23
Luo, J.-W., Wang, F.-F., Zhu-Ge, J.-M., et al. 2023, ApJ, 959, 44
MacFadyen, A. I., & Woosley, S. E. 1999, ApJ, 524, 262
MacLachlan, G. A., Shenoy, A., Sonbas, E., et al. 2013, MNRAS, 432, 857
Martin-Carrillo, A., Schneider, B., Pugliese, G., et al. 2024, GCN, 37293, 1
Mazzali, P. A., Deng, J., Tominaga, N., et al. 2003, ApJL, 599, L95
MichałowskI, M. J., Xu, D., Stevens, J., et al. 2018, A&A, 616, A169
Minaev, P. Y., & Pozanenko, A. S. 2020, MNRAS, 492, 1919
Moss, M., Lien, A., Guiriec, S., Cenko, S. B., & Sakamoto, T. 2022, ApJ, 927, 157
Moss, M. J., Barthelmy, S. D., Gupta, R., et al. 2024, GCN, 37355, 1
Nakar, E. 2007, PhR, 442, 166
Negro, M., Cibrario, N., Burns, E., et al. 2025, ApJ, 981, 14
Neubert, T., Østgaard, N., Reglero, V., et al. 2019, arXiv:1906.12178
Norris, J. P. 2002, ApJ, 579, 386
Norris, J. P., Marani, G. F., & Bonnell, J. T. 2000, ApJ, 534, 248
Nuessle, P., Racusin, J. L., & White, N. E. 2024, ApJ, 974, 120
Nugent, A. E., Fong, W. F., Dong, Y., et al. 2022, ApJ, 940, 57
O'Connor, B., Busmann, M., Hall, X. J., et al. 2026, arXiv:2605.18973
O'Connor, B., Troja, E., Dichiara, S., et al. 2022, MNRAS, 515, 4890
Pandey, S. B., Hu, Y., Castro-Tirado, A. J., et al. 2019, MNRAS, 485, 5294
Peña, C., Laskar, T., Schroeder, G., et al. 2024a, GCN, 37322, 1
Peña, C., Schroeder, G., Laskar, T., et al. 2024b, GCN, 37353, 1
Poolakkil, S., Preece, R., Fletcher, C., et al. 2021, ApJ, 913, 60
Poole, T. S., Breeveld, A. A., Page, M. J., et al. 2008, MNRAS, 383, 627
Preece, R. D., Briggs, M. S., Mallozzi, R. S., et al. 2000, ApJS, 126, 19
Prentice, S. J., Mazzali, P. A., Pian, E., et al. 2016, MNRAS, 458, 2973
Qin, Y., Liang, E.-W., Liang, Y.-F., et al. 2013, ApJ, 763, 15
Qin, Y.-P., & Chen, Z.-F. 2013, MNRAS, 430, 163
Rastinejad, J. C., Gompertz, B. P., Levan, A. J., et al. 2022, Natur, 612, 223
Romanov, F. D. 2024, GCN, 37335, 1
Roming, P. W. A., Kennedy, T. E., Mason, K. O., et al. 2005, SSRv, 120, 95
Rossi, A., Rothberg, B., Palazzi, E., et al. 2022, ApJ, 932, 1
Ruffini, R., Bianco, C. L., Della Valle, M., et al. 2024, GCN, 37536, 1
Sánchez-Ramírez, R., Lang, R. G., Pozanenko, A., et al. 2024, A&A, 692, A3
Sari, R., & Piran, T. 1999, ApJ, 520, 641
Sari, R., Piran, T., & Narayan, R. 1998, ApJL, 497, L17
Savaglio, S., Glazebrook, K., & Le Borgne, D. 2006, AIPC, 836, 540
Savaglio, S., Glazebrook, K., & Le Borgne, D. 2009, ApJ, 691, 182
Schady, P., Dwelly, T., Page, M. J., et al. 2012, A&A, 537, A15
Schady, P., Mason, K. O., Page, M. J., et al. 2007, MNRAS, 377, 273
Schady, P., Page, M. J., Oates, S. R., et al. 2010, MNRAS, 401, 2773
Schlafly, E. F., & Finkbeiner, D. P. 2011, ApJ, 737, 103
Schlegel, D. J., Finkbeiner, D. P., & Davis, M. 1998, ApJ, 500, 525
Soderberg, A. M., Chakraborti, S., Pignata, G., et al. 2010, Natur, 463, 513
Srinivasaragavan, G. P., O'Connor, B., Cenko, S. B., et al. 2023, ApJL, 949, L39
Starling, R. L. C., Wiersema, K., Levan, A. J., et al. 2011, MNRAS, 411, 2792
Stratta, G., Nicuesa Guelbenzu, A. M., Klose, S., et al. 2025, ApJ, 979, 159
Sun, H., Wang, C. W., Yang, J., et al. 2025, NSRev, 12, nwae401
SVOM/C-GFTTeam, Wu, C., Kang, Z., et al. 2024, GCN, 37373, 1
Taggart, K., & Perley, D. A. 2021, MNRAS, 503, 3931
Tanga, M., Krühler, T., Schady, P., et al. 2018, A&A, 615, A136
Troja, E., Fryer, C. L., O'Connor, B., et al. 2022, Natur, 612, 228
Uhm, Z. L., & Zhang, B. 2014, ApJ, 780, 82
Ukwatta, T. N., Stamatikos, M., Dhuga, K. S., et al. 2010, ApJ, 711, 1073
Valenti, S., Benetti, S., Cappellaro, E., et al. 2008, MNRAS, 383, 1485
van Dokkum, P. G. 2001, PASP, 113, 1420
van Eerten, H. J., & Wijers, R. A. M. J. 2009, MNRAS, 394, 2164
Veres, P., Bhat, P. N., Burns, E., et al. 2023, ApJL, 954, L5
Volnova, A., Pozanenko, A., Mazaeva, E., et al. 2021, AnABC, 93, e20200883
von Kienlin, A., Meegan, C. A., Paciesas, W. S., et al. 2020, ApJ, 893, 46
Wang, B. T., Song, F. F., Li, R. Z., et al. 2024, GCN, 37306, 1
Wang, C.-W., Tan, W.-J., Xiong, S.-L., et al. 2025, ApJL, 985, L30
Wang, X. I., Zhang, B.-B., & Lei, W.-H. 2022, ApJL, 931, L2
Woosley, S. E. 1993, ApJ, 405, 273
Woosley, S. E., & Bloom, J. S. 2006, ARA&A, 44, 507
Wu, C., Wang, Y., Li, H.-L., et al. 2025, arXiv:2507.02806
Yang, J., Ai, S., Zhang, B.-B., et al. 2022, Natur, 612, 232
Yang, Y.-H., Troja, E., O'Connor, B., et al. 2024, Natur, 626, 742
Zhang, B. 2025, JHEAp, 45, 325
Zhang, B., & Kobayashi, S. 2005, ApJ, 628, 315
Zhang, Z.-B., Yang, E.-B., Choi, C.-S., & Chang, H.-Y. 2016, MNRAS, 462, 3243
Zhang, B., Zhang, B.-B., Virgili, F. J., et al. 2009, ApJ, 703, 1696
Zhu, S.-Y., Sun, W.-P., Ma, D.-L., & Zhang, F.-W. 2024, MNRAS, 532, 1434